Exploring the drivers of global and local sea-level change over the 21st century and beyond

Earth's Future

RESEARCH ARTICLE
10.1029/2019EF001413

Exploring the Drivers of Global and Local Sea-Level Change Over the 21st Century and Beyond

M. D. Palmer[1], J. M. Gregory[1,2], M. Bagge[3], D. Calvert[1], J. M. Hagedoorn[4], T. Howard[1], V. Klemann[3], J. A. Lowe[1], C. D. Roberts[1,5], A. B. A. Slangen[6], and G. Spada[7]

[1]Met Office Hadley Centre, Exeter, UK, [2]University of Reading, Reading, UK, [3]Helmholtz Centre Potsdam, GFZ German Research Centre for Geosciences, Potsdam, Germany, [4]University of Potsdam, Potsdam, Germany, [5]Now at ECMWF, Reading, UK, [6]Royal Netherlands Institute for Sea Research, Texel, The Netherlands, [7]Università degli Studi di Urbino "Carlo Bo", Urbino, Italy

Abstract We present a new set of global and local sea-level projections at example tide gauge locations under the RCP2.6, RCP4.5, and RCP8.5 emissions scenarios. Compared to the CMIP5-based sea-level projections presented in IPCC AR5, we introduce a number of methodological innovations, including (i) more comprehensive treatment of uncertainties, (ii) direct traceability between global and local projections, and (iii) exploratory extended projections to 2300 based on emulation of individual CMIP5 models. Combining the projections with observed tide gauge records, we explore the contribution to total variance that arises from sea-level variability, different emissions scenarios, and model uncertainty. For the period out to 2300 we further breakdown the model uncertainty by sea-level component and consider the dependence on geographic location, time horizon, and emissions scenario. Our analysis highlights the importance of local variability for sea-level change in the coming decades and the potential value of annual-to-decadal predictions of local sea-level change. Projections to 2300 show a substantial degree of committed sea-level rise under all emissions scenarios considered and highlight the reduced future risk associated with RCP2.6 and RCP4.5 compared to RCP8.5. Tide gauge locations can show large (> 50%) departures from the global average, in some cases even reversing the sign of the change. While uncertainty in projections of the future Antarctic ice dynamic response tends to dominate post-2100, we see substantial differences in the breakdown of model variance as a function of location, time scale, and emissions scenario.

Key Points:
- We have developed a new set of global and local sea-level projections for the 21st century and extended to 2300 that are rooted in CMIP5 climate model simulations, including more comprehensive treatment of uncertainty than previously reported in IPCC AR5
- Analysis of local sea-level projections and tide gauge data suggests that local variability will dominate the total variance in sea-level change for the coming decades at all locations considered
- The extended sea-level projections highlight the substantial multicentury sea-level rise commitment under all RCP scenarios and the dependence of modeling uncertainty on geographic location, time horizon, and climate scenario

Supporting Information:
- Supporting Information S1
- Figure S1
- Figure S2
- Figure S3
- Figure S4
- Figure S5
- Figure S6
- Figure S7
- Figure S8

Correspondence to:
M. D. Palmer,
matthew.palmer@metoffice.gov.uk

Citation:
Palmer, M. D., Gregory, J. M., Bagge, M., Calvert, D., Hagedoorn, J. M., Howard, T., et al. (2020). Exploring the drivers of global and local sea-level change over the 21st century and beyond. *Earth's Future*, *8*, e2019EF001413. https://doi.org/10.1029/2019EF001413

Received 7 NOV 2019
Accepted 12 JUN 2020
Accepted article online 18 JUN 2020

1. Introduction

The IPCC Special Report on Oceans and Cryosphere in a Changing Climate (SROCC) estimates that global-mean sea level (GMSL) increased by 0.16 ± 0.05 m over the period 1902–2015 (IPCC, 2019). Furthermore, GMSL rise is accelerating: The estimated rate for 2006–2015 (3.6 mm yr^{-1}) is about 2.5 times the rate for 1901–1990 (1.4 mm yr^{-1}) with the contribution from melting ice sheets and glaciers exceeding that of thermal expansion for the recent period. Sea-level rise exacerbates extreme sea-level events and coastal hazards and has numerous adverse impacts on marine coastal ecosystems (IPCC, 2019). Information on future sea-level rise is therefore a key component for climate change impacts studies and informing coastal decision makers, particularly for adaptation planning.

A number of recent studies have considered potential future changes in both local mean sea-level change and drivers of extreme sea-level events (such as waves and storm surges) to explore changes in future coastal flood risk (e.g., Cannaby et al., 2016; Howard et al., 2019; Vousdoukas et al., 2018). While changes in the drivers of extreme sea levels can make a substantive contribution, the overwhelmingly dominant factor in projections of future coastal flood risk is mean sea-level rise, which results primarily from melting of land-based ice and the expansion of seawater as the oceans warm (Church et al., 2013). Therefore, the work presented here focuses on projections of mean sea-level change at global and local scales. Throughout the manuscript, we adopt the sea-level nomenclature and definitions recently put forward by Gregory et al. (2019).

The sea-level projections presented here have their origins in research carried out as part of UKCP18 (Lowe et al., 2018), a government-funded project to deliver state-of-the-art climate projections primarily for the United Kingdom. Detailed methods on the UKCP18 sea-level projections, including consideration of changes in surges, tides, and coastal waves, are described in Palmer, Howard, et al. (2018), with a synthesis of the

results for the 21st century presented by Howard et al. (2019). The UKCP18 mean sea-level projections were rooted in the CMIP5 model simulations and Monte Carlo approach used for GMSL projections in the IPCC 5th Assessment Report of Working Group I (Church et al., 2013; hereafter, AR5), with several extensions and innovations, as described below.

First, the contribution to future GMSL rise from dynamic ice input from Antarctica was updated based on the scenario-dependent projections from Levermann et al. (2014). Second, a scaling approach was adopted for local projections of sterodynamic sea-level change that better isolates the forced response from internal variability (e.g., Bilbao et al., 2015; Perrette, Landerer, Riva, Frieler, & Meinshausen, 2013). Third, the AR5 Monte Carlo approach was extended to the local sea-level projections to ensure traceability to the GMSL projections and preserve the correlations among the different terms. Fourth, a more comprehensive treatment of uncertainty was devised, by including several different estimates of (i) the sea-level change associated with glacial isostatic adjustment (GIA) and (ii) the barystatic-GRD fingerprints, that is, the spatial patterns of sea-level change associated with projections of land-based ice loss that arise from gravitational, rotational, and deformation effects. Note that the term "GRD" has been introduced by Gregory et al. (2019). Previously these effects have been referred to as the "sea-level equation" or "(gravitational) fingerprints," for example.

In addition, UKCP18 provided an additional set of projections based on an emulated ensemble of CMIP5 models that extend to 2300 (Palmer, Harris, et al., 2018). These exploratory projections have a high degree of consistency with the UKCP18 21st century projections and maintain traceability to the CMIP5 models. The methods presented here are almost identical to those used for UKCP18 and described by Palmer, Howard, et al. (2018). Here, we make use of global GIA estimates, rather than regional solutions developed specifically for the United Kingdom. Only two of the three sets of GRD "fingerprints" presented here were available for UKCP18, but this limitation does not make any substantive difference to the results (see section 4). Whereas UKCP18 considered only local sea-level projections for the United Kingdom, this study is global in scope, and we include new analysis of the drivers of variance for both GMSL and local projections.

The local sea-level projections presented here correspond to a limited number of example tide gauge locations around the world. These locations are selected based on the availability of tide gauge records long enough to estimate local sea-level variability and to span a range of future projection regimes that illustrate important geographic differences. While we also make use of satellite altimeter observations, tide gauge records are particularly useful for estimating local interannual variability owing to thelonger records available and more direct monitoring of coastal sea level. In addition, tide gauge records include vertical land motion associated with glacial isostatic adjustment—a process included in our projections but absent from satellite altimeter observations. The focus on a limited set of tide gauges allows a deeper exploration of the drivers and uncertainties in future local sea-level change through computation of the covariance matrix of our large Monte Carlo simulations.

Since the publication of AR5 several studies have highlighted the need for more comprehensive information on potential future sea-level change "tail risk" to complement IPCC-like sea-level projections that characterize the central part of the probability distribution, in order to facilitate effective coastal planning (e.g., Hinkel et al., 2019; Stammer et al., 2019). This requirement has motivated the development of probabilistic projections that aim to provide more comprehensive information on the projected probability density functions (PDFs; e.g., Garner et al., 2018; Jevrejeva et al., 2019). However, probabilistic sea-level projections are sensitive to the assumptions made about the tails of the PDFs. For example, using different methods, both Kopp et al. (2014) and Jackson and Jevrejeva (2016) drew on the expert elicitation study of Bamber and Aspinall (2013) to introduce non-Gaussian uncertainty into the tails of Greenland and Antarctic ice sheet contributions. The substantial differences in their PDFs of projected global and local sea-level at 2100 (Jevrejeva et al., 2019) are indicative of the uncertainty associated with our understanding of key ice sheet processes and low scientific confidence in the extreme percentiles.

An alternative approach to exploring tail risk is through consideration of possible high-end scenarios of future sea-level rise (Stammer et al., 2019), such as the "H++" scenario developed for UKCP09 (Lowe et al., 2018). Shepherd et al. (2018) suggested an event-orientated storyline approach with no requirement for a priori probability assessment. Ideally, these physicallybased narratives should be testable with future observations (e.g., marine ice cliff instability; DeConto & Pollard, 2016) and can be a useful framework to aid the communication and interpretation of risk. The UKCP18 Marine Report (Palmer, Howard,

Figure 1. Locations of tide gauge data used in this study. The same locations are used for extraction of satellite altimeter observations and the local sea-level projections presented in section 4.2.

et al., 2018) recommended that information from high-end scenarios be used alongside climate-model-derived sea-level projections, such as those presented here, to more fully sample future possibility space (Rohmer, Le Cozannet, & Manceau, 2019).

The outline of the paper is as follows. In section 2 we describe the observational and model data used in this study and present the tide gauge locations used for our local sea-level projections. In section 3 we present an overview of the methods used in our global and local sea-level projections. GMSL projections are presented in section 4.1, including a breakdown of the component uncertainties and discussion of the correlations among the different components. In section 4.2 we present sea-level projections at several tide gauge locations and explore the relative importance of variability, scenario, and model uncertainty over the 21st century following Hawkins and Sutton (2009). Section 4.3 focuses on model uncertainty and how the breakdown of total variance into the different components varies by geographic location, scenario, and time scale. Finally, in section 5, we discuss our key findings and present a summary.

2. Data

2.1. Tide Gauge Data

The local sea-level projections presented in section 4.2 are premised on several example tide gauge locations around the world (Figure 1). These locations are chosen to span a range of future sea-level change regimes and to provide reasonable tide gauge time series with which to estimate the local interannual variability. Data are sourced from the Permanent Service for Mean Sea Level (Holgate et al., 2013; https://www.psmsl.org/). The latitude and longitude of each tide gauge location are summarized in Table S1. The tide gauge records used have not been corrected for vertical land motions. This is appropriate, since our local sea-level projections include an estimate of local glacial isostatic adjustment (GIA), and therefore, we do not want to remove this signal from the tide gauge record.

2.2. Satellite Altimeter Data

The satellite altimeter data used in this study come from v2.0 of the European Space Agency (ESA) Climate Change Initiative for observations of sea level (http://www.esa-sealevel-cci.org), as described by Legeais et al. (2018). This data product is based on reprocessed and homogenized gridded observations from nine altimeter missions over the period 1993–2015 and provides monthly mean values for GMSL and two-dimensional fields on a ¼ × ¼° latitude-longitude grid. Monthly mean timeseries of GMSL anomaly are converted to annual means for comparison with our projections of GMSL. Similarly, we convert monthly mean two-dimensional fields of gridded sea-level anomaly to annual-mean values. We extract the annual-mean time series from the closest available grid box to the tide gauge locations shown in Figure 1.

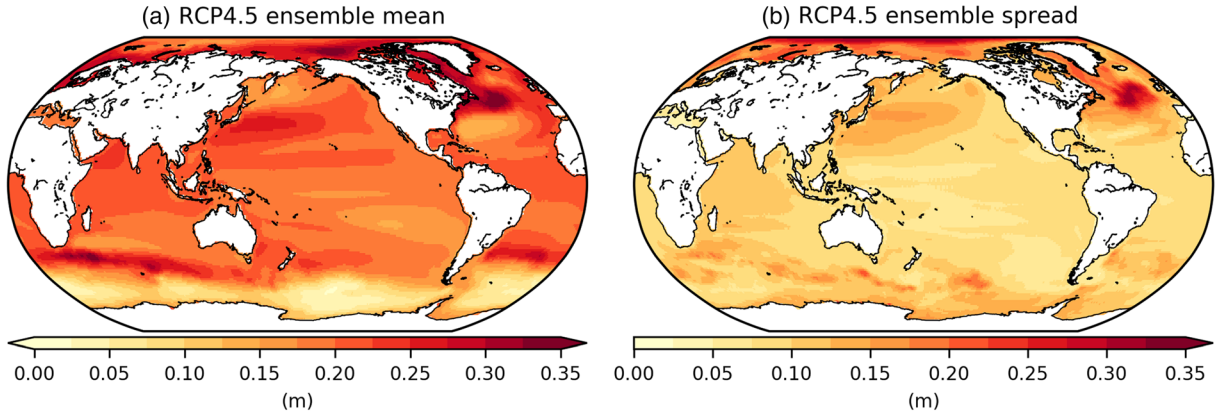

Figure 2. Projections of sterodynamic sea level change for the period 2081–2100 relative to the 1986–2005 average from an ensemble of 21 CMIP5 models: (a) ensemble mean; (b) ensemble spread (90% confidence interval based on the ensemble standard deviation). The spatial patterns arise from the forced response of ocean dynamic sea level across the CMIP5 ensemble. Adapted from IPCC AR5 (Church et al., 2013; Figure 13.16).

The only exception to this is for Palermo, where we select values from two grid boxes further east in order to avoid apparent data issues that may be associated with land-proximity effects.

2.3. CMIP5 Data

The sea-level projections presented in this study are rooted in climate model simulations carried out as part of the Coupled Model Intercomparison Project Phase 5 project (CMIP5; Taylor et al., 2012). A full list of the CMIP5 models used and their various applications is summarized in Table S2.

The 21st century projections presented here are based on the same CMIP5 model ensemble as used for the GMSL projections presented in AR5. These projections make use of simulations of global-mean surface temperature (*tas*) and global-mean thermosteric sea-level (*zostoga*) rise from 21 CMIP5 models under the representative concentration pathway climate change scenarios (RCPs, Meinshausen et al., 2011). Time series of *zostoga* have been drift-corrected using a quadratic fit to the corresponding pre-industrial control simulation for each model. This step is performed to remove any artificial signals associated with ongoing spin-up deep ocean and/or limitations in the representation of energy conservation in the model domain, as discussed by Sen Gupta et al. (2013) and Hobbs et al. (2016). Further information is provided in the supplementary materials of AR5 (Church et al., 2013).

Our extended sea-level projections to 2300 are based on an ensemble of two-layer energy balance model (TLM) simulations with parameter settings that have been tuned to emulate the forced response of individual CMIP5 models in idealized CO_2 experiments models following Geoffroy et al. (2013). This ensemble also provides time series of *tas* and *zostoga* under the extended RCP scenarios (Meinshausen et al., 2011), and it is based on 14 CMIP5 models, with 11 models common to the AR5 CMIP5 ensemble. Full details of the methods and evaluation of the TLM simulations are described by Palmer, Harris, et al. (2018).

At regional scales, changes in ocean dynamic sea level (arising from changes in ocean circulation and/or density) are important determinants of local sea-level change. To account for this, we make use of CMIP5 model simulations of global-mean thermosteric sea level (*zostoga*) and ocean dynamic sea level (*zos*) from 21 CMIP5 models under the RCP climate change scenarios. Following previous studies (Cannaby et al., 2016; Palmer, Howard, et al., 2018), both *zostoga* and *zos* are drift-corrected using a linear fit to the corresponding pre-industrial control simulations. These data are then used to establish regression relationships between the local sterodynamic sea-level change (*zostoga* + *zos*) and global-mean thermosteric sea-level change (*zostoga*) across the CMIP5 ensemble at each tide gauge location.

The spatial pattern of sterodynamic sea-level change is illustrated for RCP4.5 (Figure 2). The characteristic multimodel mean response includes an increase in sea-level gradient across the Southern Ocean and enhanced sea-level rise in the North Atlantic and Arctic Oceans. The multimodel spread is largest in the North Atlantic and Arctic Oceans. Analysis of AOGCM experiments conducted for the flux-anomaly-forced model intercomparison project (FAFMIP, Gregory et al., 2016) shows that the change in the Southern Ocean

is due to a combination of increases in wind stress and heat input, in the North Atlantic due to reduced heat loss and the consequent weakening of the Atlantic meridional overturning circulation (especially along the North American coast; Bouttes et al., 2014; Yin et al., 2009), and in the Arctic due to increased freshwater input from precipitation and river inflow.

2.4. GRD Estimates

Changes in the amount of ice and water stored on land give rise to spatial patterns of mean sea-level (MSL) change associated with the effects on Earth's gravity, rotation, and solid earth deformation (e.g., Tamisiea & Mitrovica, 2011). Gregory et al. (2019) refer to these effects collectively as GRD (Gravity, Rotation, Deformation), and we adopt their nomenclature here. We use three different estimates of GRD for the different ice mass terms following Slangen et al. (2014), Spada and Melini (2019), and Klemann and Groh (2013) extended to include rotational deformation following Martinec and Hagedoorn (2014). We use a single GRD estimate for changes in land water storage based on the projections of Wada et al. (2012), following Slangen et al. (2014). The geographic distributions of mass change for each component come from Slangen et al. (2014). Note that, while our results incorporate some uncertainty arising from different GRD model solutions, they do not account for uncertainties in the geographic distribution of mass change. Further details on the GRD calculations are available in the supporting information.

The GRD estimates are expressed as the local MSL change per unit GMSL rise from each of the following barystatic (i.e., GMSL mass addition/loss) terms: (i) Antarctic surface mass balance, (ii) Antarctic ice dynamics, (iii) Greenland surface mass balance, (iv) Greenland ice dynamics, (v) worldwide glaciers, and (vi) changes in land water storage (Figure 3). Loss of ice from the Antarctic and Greenland ice sheets are characterized by a near-field MSL fall and a greater-than-unity rise in the far-field (e.g., Figures 3a and 3g), with notable differences in the GRD estimates for surface mass balance and ice dynamics, owing to different geographic distributions of mass change. The GRD estimates associated with worldwide glaciers and land water storage are spatially more complex, owing to the more geographically widespread mass distributions (Figures 3c and 3i). The glacier GRD pattern assumes a fixed distribution of the ratios of glacier mass loss between the glacier regions based on the projected distribution in 2100 under RCP8.5 (Church et al., 2013). Previous analysis showed that this pattern does not vary much over the 21st century and the amount of mass closely related to the initial glacier mass for a given region. We acknowledge that this is a simplistic approach, and recent studies have shown that the mass loss distribution to be model and scenario dependent (Hock et al., 2019). For the local sea-level projections presented here, we expect the uncertainty in the total glacier contribution to dominate. However, future sea-level projections could be improved by more comprehensive representation of the uncertainties associated with the spatial pattern of future glacier mass loss.

The spatial patterns of GRD can have an important impact on projections of local MSL change. Depending on the geographic location, components of GMSL change can be greatly attenuated (if the location is close to where the GRD pattern is zero) and even result in a change of sign of one or more components (where the GRD pattern has negative values).

Computing the standard deviations across the three GRD estimates shows that differences are largest in the regions of ice/water mass loss (Figures 3d–3f, 3j, and 3k), corresponding to the negative value regions seen in the mean GRD patterns (Figures 3a–3c and 3g–3i). Away from these areas, the agreement among GRD estimates is high, with the standard deviation representing only a few % of the local mean signal. The circular spatial structures seen in the panels of standard deviation for the Greenland components (Figures 3j and 3k) and Antarctic ice dynamics (Figure 3e) resemble a 2-1 pattern of spherical harmonics and are indicative of slight differences in the rotational effects among the three estimates. Although all three estimates are based on the same well-understood physics, differences arise from the methods used to compute the Love numbers, as well as different grid formulations and spatial resolutions to solve the convolution integral (Table S3; see Martinec et al., 2018, for a discussion). From a practical standpoint, we find that the small differences among estimates lead to a negligible uncertainty for the tide gauge locations considered here, compared to the other factors (see section 4.3). For future studies that consider regions in closer proximity to the ice mass changes, increasing the spatial resolution would promote greater consistency among the GRD estimates.

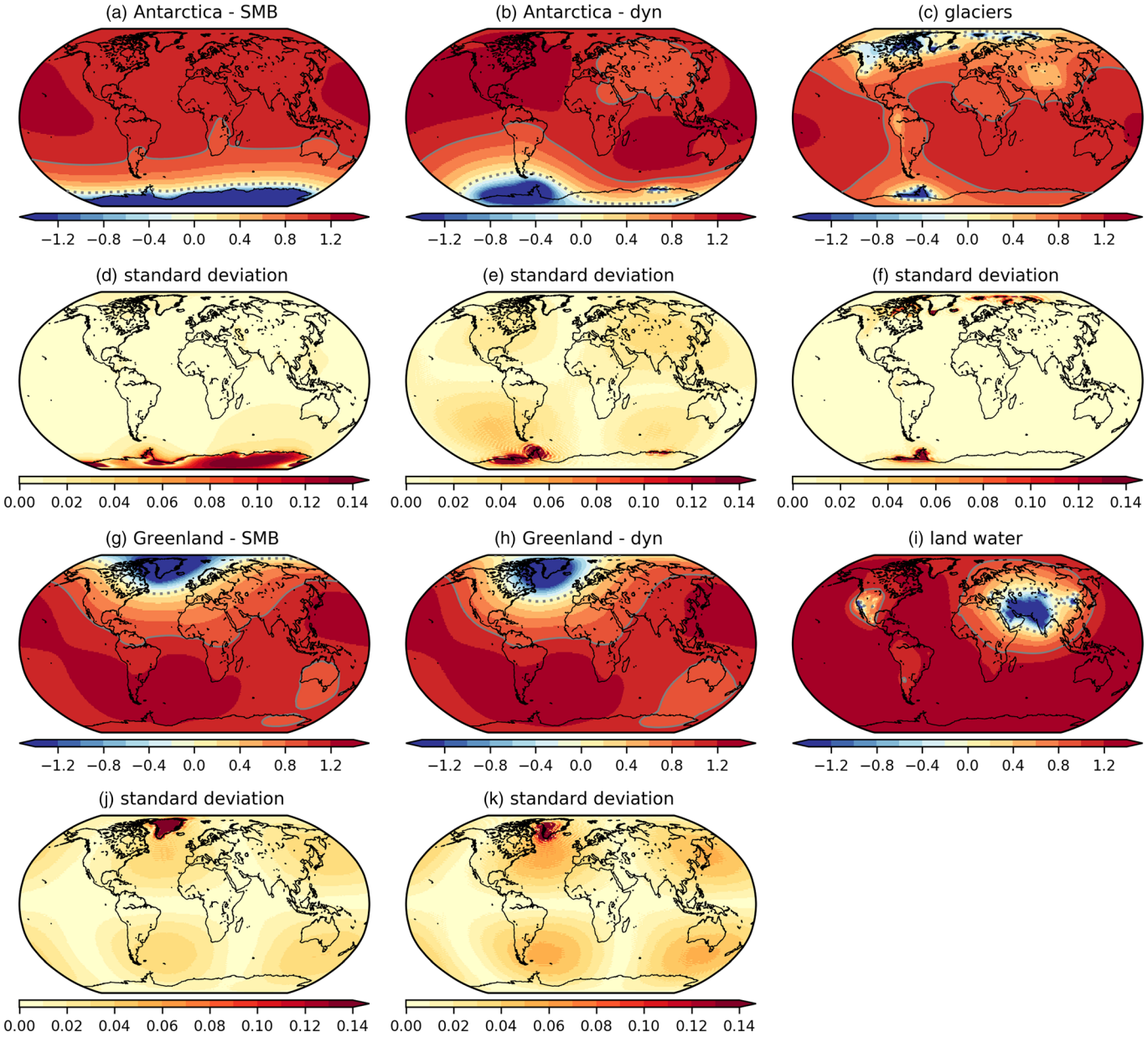

Figure 3. Estimates of the combined effect of mass changes on Earth's gravity, rotation, and solid earth deformation (GRD) on local relative sea level. Panels (a), (b), (c), (g) and (h) show the mean of three sets of estimates with corresponding standard deviations across estimates shown in (d), (e), (f), (j) and (k). only a single estimate was available for land water, and therefore, no standard deviation is shown. GRD estimates are expressed as the ratio of local MSL to GMSL per unit rise/fall with the 1:1 and zero contours indicated by the solid and dotted gray lines, respectively.

2.5. Glacial Isostatic Adjustment

Similar to the effects of GRD discussed in the previous section, ongoing glacial isostatic adjustment (GIA) also leaves its imprint in the spatial pattern of MSL change. GIA is associated with the adjustment of Earth's lithosphere and viscous mantle material to past changes in ice loading since the last glaciation (e.g., Tamisiea & Mitrovica, 2011). This adjustment process gives rise to areas of upward and downward vertical land motion, and the associated mass redistribution also influences Earth's rotation and gravity field with additional impacts on local MSL. It is well known that GIA leads to substantial spatial variations in the rates of MSL change observed at tide gauges and, such as the lower rate of sea-level rise seen for the north of the United Kingdom compared to the south (Howard et al., 2019; Palmer, Harris, et al., 2018). Since the adjustment time

scales of GIA are thousands of years, we make the approximation that the contemporary rates of its effect on local MSL change are valid for the projections (i.e., the rates are assumed to be time constant).

We use three global GIA estimates in this study. The first is based on the ICE-5G (VM2 L90) model (Peltier, 2004). The second is based on ICE-6G_C (VM5a) (Argus et al., 2014; Peltier et al., 2015). ICE-6G_C is a refinement of the ICE-5G model, based on a wider range of observational constraints, including new data from Global Positioning System (GPS) receivers and as time-dependent gravity observations from both surface measurements and the satellite-based Gravity Recovery and Climate Experiment GRACE (Peltier et al., 2015). Peltier et al. (2015) state that the GIA solution from ICE-6G_C uses an improved ice loading history compared to ICE5G. Both of these data sets were sourced from http://www.atmosp.physics.utoronto.ca/~peltier/data.php. The final global GIA data product represents an independent estimate from the Australian National University based on an update of Nakada and Lambeck (1988) in 2004–2005. This final GIA estimate is identical to that used by Slangen et al. (2014). All three GIA data sets are provided on a $1 \times 1°$ latitude-longitude grid.

There are substantial differences among all three GIA estimates, despite ICE5G and ICE6G originating from the same modeling group. The overall spread in GIA estimates is largest for areas of North America, the Arctic, and Antarctica, that is, the regions of large ice mass changes during the last deglaciation. A detailed comparison and explanation for the differences is beyond the scope of this paper. A major limitation in GIA modeling is the lack of 3-D earth structures together with glaciation histories which in combination can be constrained locally against observational data. However, the optimized global 1-D estimates presented here represent a compromise, and therefore, our study may tend to overestimate the GIA uncertainty compared to locally optimized solutions. For example, UKCP18 used a regional, observationally constrained GIA solution with substantially smaller estimated uncertainties reported here (Howard et al., 2019; Palmer, Howard, et al., 2018).

3. Methods

3.1. Global-Mean Sea-Level Projections

The local MSL projections presented here are based on 21st century process-based projections of GMSL presented in IPCC AR5 (Church et al., 2013). The GMSL projections are composed of seven components: (i) global-mean thermosteric sea level; and barystatic sea level due to (ii) Antarctic surface mass balance; (iii) Antarctic ice dynamics; (iv) Greenland surface mass balance; (v) Greenland ice dynamics; (vi) worldwide glaciers; and (vii) net changes in land water storage. The first component is also referred to as "global thermal expansion" and is the only term that does not constitute a change in ocean mass following Gregory et al. (2019).

For the period out to 2100, the GMSL projections are underpinned by 21 CMIP5 climate model simulations (Taylor et al., 2012) of global thermal expansion (GTE) and global-mean surface temperature (GMST) change under the Representative Concentration Pathway (RCP) climate change scenarios (Meinshausen et al., 2011). For the extended period out to 2300 we use projections of GTE and GMST change from a physically based emulator that has been tuned to 16 CMIP5 models (Palmer, Harris, et al., 2018) under the RCP extensions (Meinshausen et al., 2011). Of the two sets of CMIP5 models, 11 are common across both the 21st century projections and the extended 2300 projections (Table S2).

Note that the extended projections were not included in AR5 and represent one of the novel aspects of this study. We stress here that there is a much greater degree of uncertainty associated with the extended projections to 2300 than for the 21st century projections. For example, the RCP extensions make very simple assumptions about emissions trajectories, and there is deep uncertainty associated with the response of ice sheets on multicentury time scales (e.g., Edwards et al., 2019). While we present the two time horizons alongside each other for reader convenience, the extended 2300 projections should be regarded with a lower degree of confidence and treated as illustrative of the potential changes.

While AR5 included scenario-independent projections of Antarctic ice dynamics based on the assessed literature, we use a parameterization of scenario-dependent projections presented by Levermann et al. (2014). This procedure is based on temperature-dependent log-normal fits to the percentiles from probability distribution functions for the sea-level contribution at 2100 for each scenario (Levermann et al., 2014; Table 6,

"shelf models" with time delay). All percentiles are reproduced to within ±0.01 m by our fits, except that the 95th percentile for RCP2.6 is slightly too high (0.26 m for the fit compared to 0.23 m in their table). We use the parameterized 5th to 95th percentile ranges at 2100 with the time dependence obtained as in the AR5 (Church et al., 2013; 13.SM1.6). Recent work has highlighted the potential importance of self-sustaining dynamic ice feedbacks (DeConto & Pollard, 2016), which are not explicitly accounted for in Levermann et al. (2014). However, the Levermann et al. (2014) study yields a similar projected range to other recent studies that do include these effects (Edwards et al., 2019). In addition, a recent analysis suggests that the likelihood of rapid acceleration of dynamic ice loss from West Antarctica simulated by DeConto and Pollard (2016) was overestimated (Edwards et al., 2019).

We follow the same approach as AR5 in constructing a 450,000-member Monte Carlo simulation for each RCP scenario that forms the basis of both the GMSL and local MSL projections. The methods used for each component and for our two different time horizons are summarized in Table 1. With the exception of changes in Greenland ice dynamics and land water storage, all GMSL components are dependent on the climate change scenario. The scenario-independent projections have ranges based on the literature assessed in AR5.

For the scenario-dependent terms, the ensemble spread arises from differences among the underlying CMIP5 (or emulator) simulations of GTE and GMST change and from any additional methodological uncertainties (Church et al., 2013). For each scenario, the climate model ensemble (CMIP5 or emulator) was treated as a normal distribution, with time-dependent ensemble mean $Q_M(t)$ and standard deviation $Q_S(t)$, where Q is GTE or GMST, both with respect to the time mean of 1986–2005, and t is time. Larger Monte Carlo ensembles were constructed with members $Q_i(t) = Q_M(t) + r_i Q_S(t)$, where $\{r_i\}$ is a set of normal random numbers (with zero mean and unit standard deviation). The $\{r_i\}$ are time-independent, and the same $\{r_i\}$ were used for GTE and GMST, so that variations within the ensemble were correlated over time and between the two quantities.

The glacier contribution to GMSL is based on a relationship between the global glacier contribution and GMST change (Church et al., 2013), which is also applied post-2100. The total contribution is capped at 0.32 m, based on current estimates of total glacier mass (Farinotti et al., 2019; Grinsted, 2013). However, we note that this is a simplistic assumption. It is possible that remaining glaciers might reach a new steady state under a stable future climate following preferential loss of low-altitude ablation areas, a possibility that was not accounted for in the AR5 projections, or here.

The different GMSL components are combined using a 450,000-member Monte Carlo simulation that samples from the underlying distributions. The procedure preserves the correlation between GTE and GMST change in the underlying CMIP5 model simulations (or the emulator ensemble for the period post-2100). As a result, many of the GMSL components are correlated, as discussed further in section 4. In addition, the effect of increased accumulation on the dynamics of the Antarctic ice sheet is represented in the same way as described in AR5 (Church et al., 2013; SM1.5), resulting in these terms also being weakly correlated. The sampled distributions are based on the 5th to 95th percentile ranges of the climate model simulations and literature-based assessed ranges for the scenario-independent terms. Each member of the Monte Carlo simulation is composed of a time series for each of the seven GMSL contributions listed in Table 1 with the correlations between terms preserved.

3.2. Local Sea-Level Projections

As we move to local MSL projections, a number of additional processes are taken into account. First, the spatial patterns of MSL change associated with each of the barystatic GMSL contributions (Table 1, ii–vii) are incorporated using estimates of the effects on Earth's gravity, rotation, and solid earth deformation (GRD, Figure 3). Following previous studies (Bilbao et al., 2015; Palmer, Howard, et al., 2018; Perrette et al., 2013), the effects of local changes in ocean density and circulation are included by establishing regression relationships between global thermal expansion and local sterodynamic sea-level change in CMIP5 climate model simulations (see supporting information, Figures S1–S4). Finally, the spatial pattern of local MSL change from ongoing glacial isostatic adjustment (GIA, Figure 4) is included in our local MSL projections.

The projections of local MSL change for specific tide gauge locations (Figure 1, Table S1) are derived directly from the GMSL Monte Carlo projections described in the previous section. This represents an advance over the local MSL projections presented in AR5 (Church et al., 2013), which combined the different components post hoc using statistical approximations (see supplementary materials of Cannaby et al., 2016; Church

Table 1
The Methods Used for Each Component of Global-Mean Sea Level (GMSL) Change According to Time Horizon

Sea-level component	21st century method	Extended 2300 method
(i) Global thermal expansion (GTE)	Projections are based on simulations with an ensemble of 21 CMIP5 models (Table S2) as described by Church et al. (2013) and in the text above. Any scenarios not available for a given model were estimated by the method of Good et al. (2013) from its other RCP and abrupt $4\times CO_2$ experiments.	Projections are based on the CMIP5-based emulator ensemble of Palmer, Harris, et al. (2018) and the corresponding CMIP5 model expansion efficiencies documented by Lorbacher et al. (2015).
(ii) Antarctica: surface mass balance	GMSL rise is projected from global-mean surface temperature (GMST) change $T(t)$ (as described by Church et al. (2013), as the time-integral of $APR(1–S)\ T(t)$, where A is the time-mean snowfall accumulation during 1985–2005, $P = 5.1 \pm 1.5\%\ °C^{-1}$ is the rate of increase of snowfall with Antarctic warming, $R = 1.1 \pm 0.2$ is the ratio of Antarctic to global warming, and S is a number in the range 0.00–0.035 that quantifies the increase in ice discharge due to increased accumulation. The Monte Carlo chooses P, R, and S independently; P and R are normally distributed and S uniformly. Projections of GMST change come from the same ensemble of 21 CMIP5 models as for GTE.	The same relationship with global surface temperature change is applied out to 2300 (Church et al., 2013). Projections of time-integral global surface temperature change come from the CMIP5-based 16-member emulator ensemble of Palmer, Harris, et al. (2018; Table S2).
(iii) Antarctica: ice dynamics	A scenario-dependent projection based on the results of Levermann et al. (2014). GMSL rise is modeled as a quadratic function of time, beginning with the observational rate of dynamic mass loss in 2006 and reaching Le^{x} at 2100, where x is chosen by the Monte Carlo from a normal distribution with zero mean and standard deviation λ. The parameters L and λ are scenario-dependent; for instance, RCP2.6 has $L = 56$ mm and $\lambda = 0.92$, RCP8.5 91 mm and 0.86.	The 2100 rate is held constant between 2100 and 2300.
(iv) Greenland: surface mass balance	GMSL rise is projected from GMST change (Church et al., 2013) as the time integral of $EFG(T(t))$, where G gives the change in Greenland SMB as a cubic function of GMST change according to Equation (2) of Fettweis et al. (2013), derived from regional climate model projections. F is a factor representing systematic uncertainty in G, and E is a factor in the range 1.00–1.15 representing the enhancement of mass loss due to reduction of surface elevation. The Monte Carlo chooses E and F independently; E is uniformly distributed, and $F = e^{N}$, where N is normally distributed with zero mean and standard deviation of 0.4. Projections of GMST change are the same as for Antarctic surface mass balance.	The 2100 rate is held constant between 2100 and 2300.
(v) Greenland: ice dynamics	Scenario-dependent projection based on the literature at the time of AR5 (Church et al., 2013). GMSL rise is modeled as a quadratic function of time, beginning with the observational rate of dynamic mass loss in 2006 and reaching 0.020–0.085 m for RCP8.5 and 0.014–0.063 m for the other RCPs at 2100. The Monte Carlo chooses the final amount uniformly within the ranges given.	The 2100 rate is held constant between 2100 and 2300.
(vi) Glaciers	GMSL rise is projected from GMST change (Church et al., 2013) as $mfI(t)^{p}$, where $I(t)$ is the time integral of GMST change (in °C yr) since 2006. Four glacier models are represented by different f,p pairs, with f in the range 3–5 mm and $p \approx 0.7$. The Monte Carlo gives equal probability to the four glacier models and chooses the random normally distributed factor m with a standard deviation of 20% representing systematic uncertainty. Projections of GMST change are the same as for Antarctic surface mass balance.	The same relationship with global surface temperature change is applied out to 2300 (Church et al., 2013) with a cap on the total sea level equivalent of 0.32 m to reflect current estimates of global glacier volume (Farinotti et al., 2019; Grinsted, 2013). Projections of global surface temperature change come from the CMIP5-based 16-member emulator ensemble of Palmer, Howard, et al. (2018; Table S2).
(vii) Land water storage	Scenario-independent projection based on the literature at the time of AR5 (Church et al., 2013). GMSL rise is modeled as a quadratic function of time, beginning with the estimated rate for 2006 and having its time-mean for 2081–2100 uniformly distributed within the range −10 to +90 mm by the Monte Carlo.	The 2100 rate is held constant between 2100 and 2300.

et al., 2013). These approximations break the correlation structure among sea-level components and compromise the traceability of the local projections, including our understanding of how the different variances combine for total sea-level change locally.

The local MSL projection Monte Carlo simulations presented here are computed as follows. For a given RCP scenario, a single instance of the 450,000-member Monte Carlo of GMSL is randomly drawn. Each instance includes a time series for the seven GMSL components that preserves the underlying correlations among them. The barystatic timeseries (Table 1, ii–vii) are combined with the corresponding GRD estimates

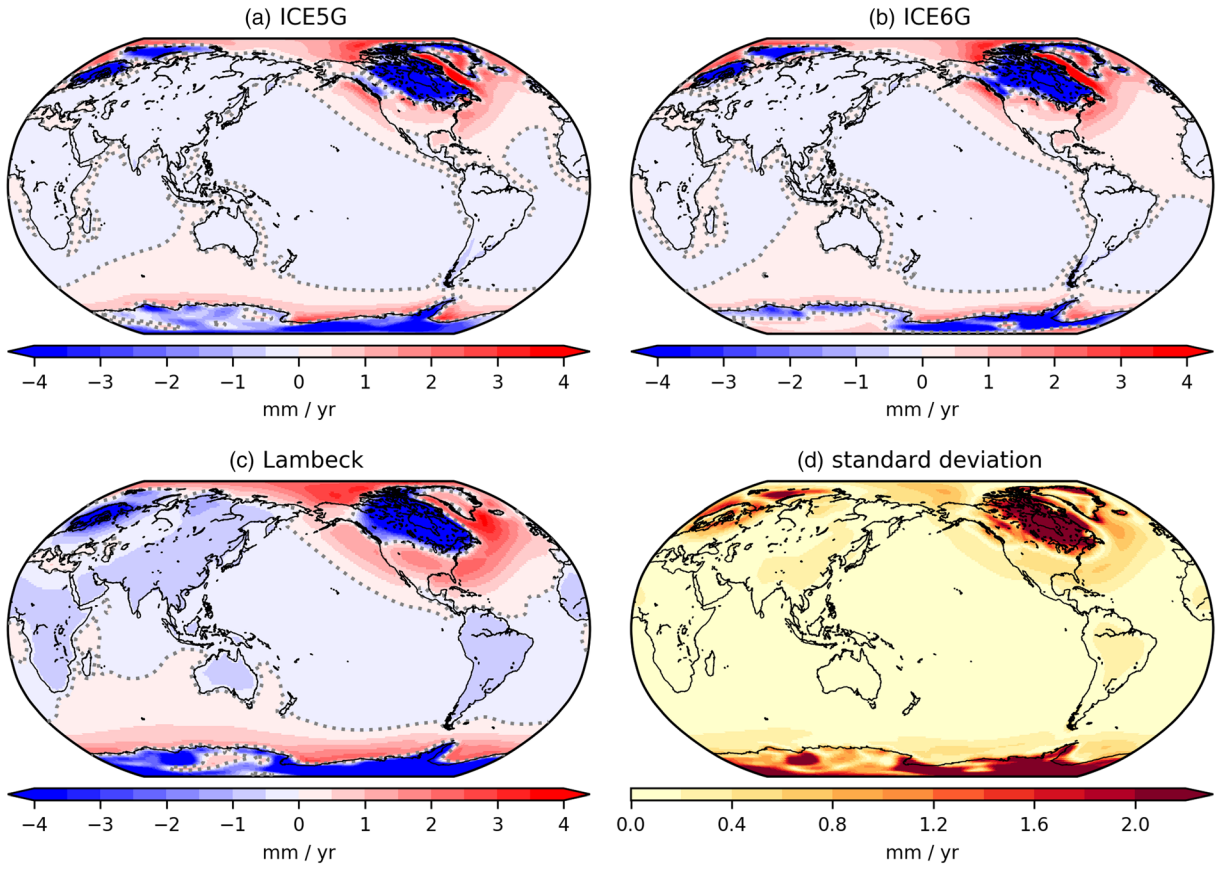

Figure 4. (a)–(c) three estimates of the effect of glacial isostatic adjustment (GIA) on sea-level change. The zero line is indicated by the dotted contours. (d) the standard deviation of the three GIA estimates. Units for all panels are mm yr^{-1}.

(Figure 3) from one of the three sets at the tide gauge latitude and longitude. This selection is made at random with all GRD patterns based on the same model, in order to preserve any correlated errors. The only exception is for land water, for which only a single GRD estimate is available (Slangen et al., 2014). The timeseries of global thermal expansion is combined with a randomly drawn regression coefficient from one of the 21 CMIP5 models in order to estimate the sterodynamic sea-level change at the tide gauge location. The resulting seven timeseries of local MSL change are then combined with an estimate of the rate of MSL change associated with GIA using one of the three estimates (Figure 4) drawn at random. This procedure (shown schematically in Figure 5) is repeated 100,000 times for each tide gauge location to build up a distribution of MSL projections under each RCP scenario. Following the approach of AR5, we take the 5th and 95th percentiles of this distribution to indicate the spread of projections for individual components and the total MSL change.

4. Results

4.1. Global-Mean Sea-Level Projections

Our projections of GMSL change show good agreement with recent observations based on satellite altimeter measurements (Figure 6). For the overlapping period of 2007–2015 the 50th percentile of the RCP4.5 projection gives the same rate as the altimeter observations of 3.8 mm per year. The observed rate of GMSL for the entire 1993–2015 period is 3.0 mm per year, indicating an acceleration over time (Nerem et al., 2018) that is also seen in the projections. For the period out to 2030 there is little difference among the projected rates of across the three RCP scenarios.

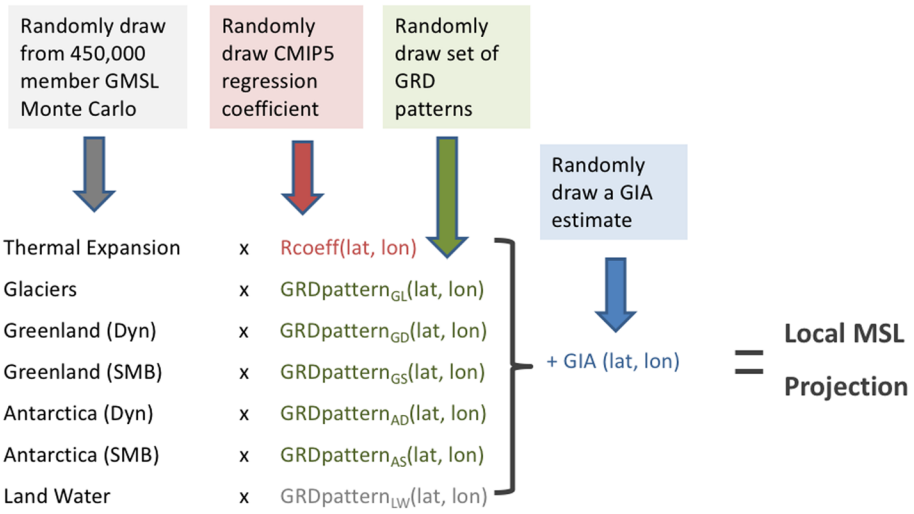

Figure 5. A schematic representation of the Monte Carlo simulation performed for the local mean sea level (MSL) projections. The above process is repeated 100,000 times to build up a distribution of sea level projections for each tide gauge location for each RCP scenario.

Our projections of GMSL change over the 21st century (Figure 7; Table 2) yield similar ranges to those presented in AR5 (Church et al., 2013) and SROCC (Oppenheimer et al., 2019). The inclusion of an updated Antarctic ice dynamics component following Levermann et al. (2014) in the present study increases the overall uncertainties and the skewness of the distribution and results in a slightly higher central estimate for RCP8.5 compared to AR5. The SROCC projections were also based on AR5, but with an updated estimate of the contribution from Antarctica based on several process-based studies (including Levermann et al., 2014). The SROCC projected ranges at 2100 are very similar to AR5, except for the RCP8.5 scenario, which is systematically higher and shows a larger uncertainty. Our extended GMSL projections show a high degree of consistency with the CMIP5-based 21st century projections evaluated at 2100 (Table 2), with all ranges agreeing to within a few centimeters.

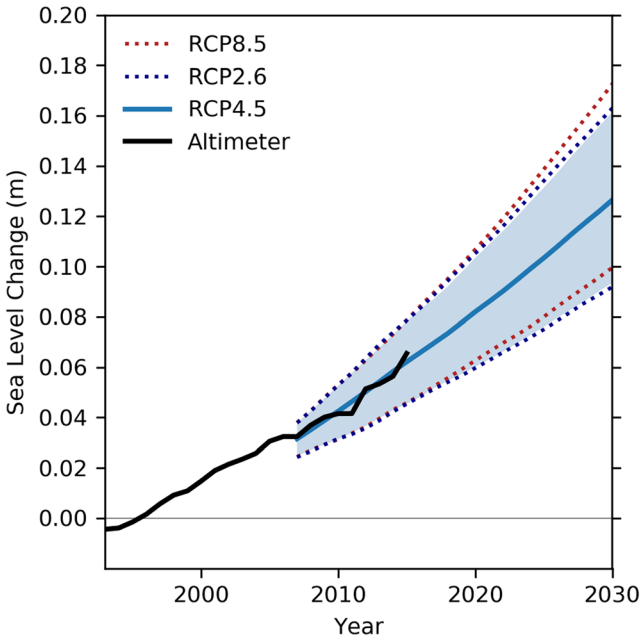

Figure 6. Comparison of satellite altimeter observations (black) with our projections of global-mean sea-level change for the period 1993 to 2030. The 50th percentile and 5th to 95th percentile range for RCP4.5 are shown by the solid line and shaded region, respectively. Also shown are the 5th and 95th percentile projections for RCP2.6 and RCP8.5 (dotted lines) as indicated in the figure legend. The satellite altimeter timeseries has been adjusted so that the mean value matches the 50th percentile of the RCP4.5 projections over the period 2007–2015.

The extended 2300 projections illustrate the long-term committed sea-level rise under all RCP scenarios and the large uncertainties associated with these time horizons. At these extended time horizons, there is a greater distinction between scenarios than for the 21st century, and the benefits of reduced greenhouse gas emissions on the potential magnitude of committed future sea-level rise are clear (cf. RCP2.6 and RCP8.5 at 2300, Table 2). For the extended 2300 projections, the total glacier ice mass becomes exhausted between 2200 and 2300 under RCP4.5 and between 2100 and 2300 under RCP8.5 (Figure 7).

Given the different methods, and the inherently large uncertainty associated with projections on multicentury time horizons, our projected values at 2300 are broadly consistent with the estimates presented in IPCC SROCC (Oppenheimer et al., 2019) and Nauels et al. (2017) (Table 2). Our results show a substantially larger projected range for RCP2.6 (0.6–2.2 m) than the SROCC likely range (0.6–1.1 m) and Nauels et al. (2017; 0.8–1.4 m). This larger range arises primarily from the Antarctica ice dynamics term (Figure 8; Figure S5) and may have important implications for adaptation planning. Both SROCC (2.3–5.4 m) and Nauels et al. (2017; 3.4–6.8 m) show higher projected ranges under RCP8.5 than the present study (1.7–4.5 m). For SROCC, these larger values arise primarily from the Antarctic component (Figure 8). For Nauels

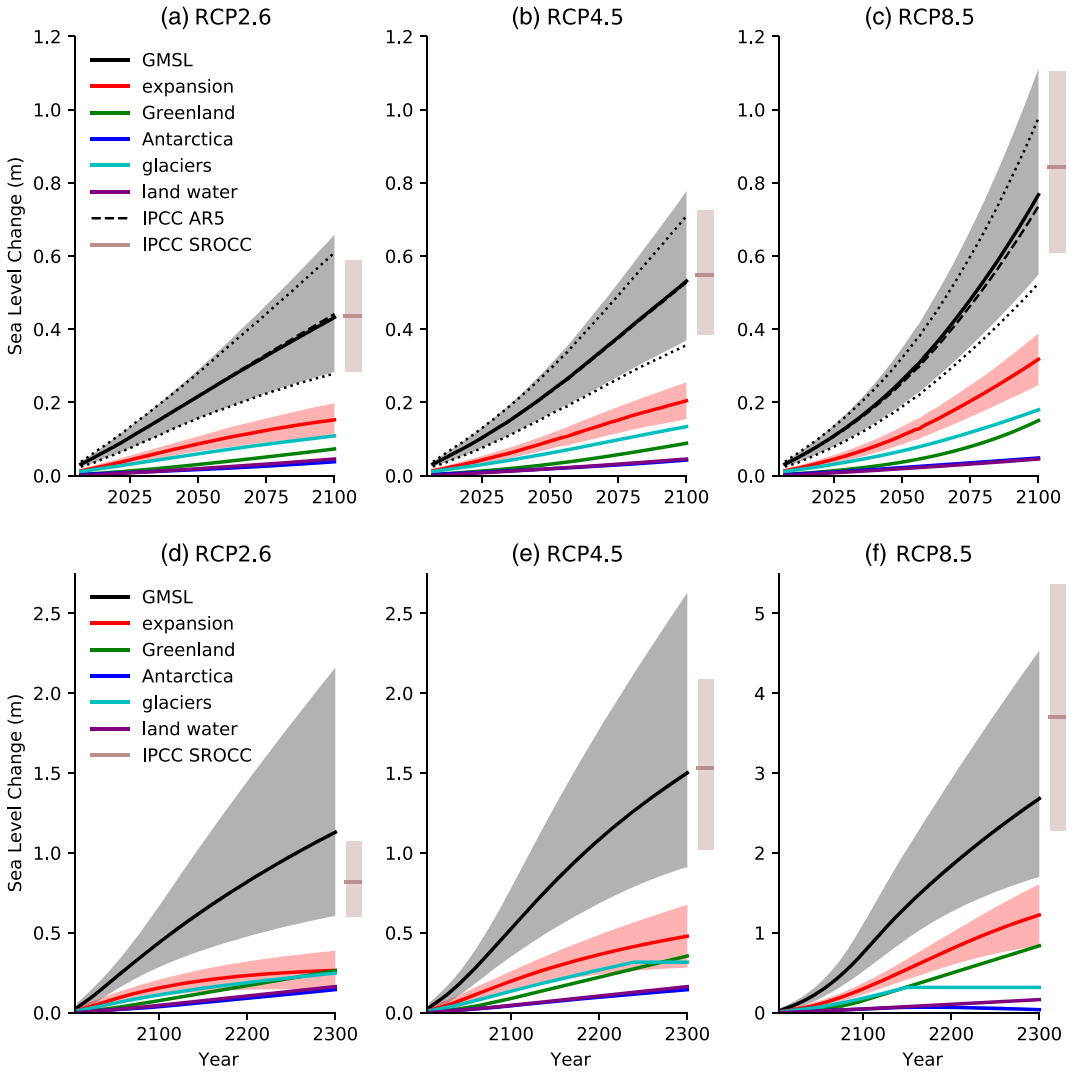

Figure 7. Projections of global-mean sea-level change for RCP2.6 (left), RCP4.5 (middle), and RCP8.5 (right) based on the 21st century methods (a–c) and the extended 2300 methods (d–f) (Table 1). Sea-level components are shown as indicated in the figure legend. The shaded regions show the 5th to 95th percentile range from the 450,000-member Monte Carlo simulation for global thermal expansion (red) and the total (gray). The dashed and dotted lines indicate the 50th percentile and 5th to 95th percentile range from the Monte Carlo simulation presented in IPCC AR5 (Church et al., 2013). The gray shaded bars on the right-hand side of each plot indicates the 5th to 95th percentile range at 2100 or 2300 from the IPCC SROCC (Oppenheimer et al., 2019). All projections are plotted relative to a baseline period of 1986–2005. Note the change of *y*-axis scale for for panel (f).

et al. (2017) the difference seems to arise from larger contributions and greater uncertainties in both global thermal expansion and Greenland surface mass balance (Figure S5).

In order to gain some initial insights into the drivers of GMSL change, we present the breakdown of components at 2100 and 2300 based on the 5th to 95th percentile range (Figure 8). For all scenarios and both time horizons, the single largest component of uncertainty is that associated with the contribution from Antarctica (combined effects of changes in surface mass balance and ice dynamics). The 5th to 95th percentile range for Antarctica includes negative values, which arises from positive surface mass balance owing to a warmer atmosphere transporting more moisture. The components and their uncertainties generally increase under the higher emissions scenarios for both time horizons. At 2100, the RCP8.5 scenario induces substantial increases in the contribution ranges for Greenland and worldwide glaciers. The exhaustion of glacier mass for the extended projections under RCP4.5 and RCP8.5 results in reduced uncertainty for this term at 2300.

Table 2
Comparison of Projected Ranges of Global-Mean Sea-Level Rise

Projection	Year	RCP2.6	RCP4.5	RCP8.5
IPCC AR5	2100	0.28–0.61 m	0.36–0.71 m	0.52–0.98 m
IPCC SROCC	2100	0.28–0.59 m	0.38–0.72 m	0.61–1.11 m
This study (21st century)	2100	0.28–0.66 m	0.37–0.78 m	0.55–1.11 m
This study (extended 2300)	2100	0.28–0.67 m	0.35–0.78 m	0.52–1.11 m
This study (extended 2300)	2200[a]	0.5–1.5 m	0.7–1.8 m	1.3–2.9 m
This study (extended 2300)	2300[a]	0.6–2.2 m	0.9–2.6 m	1.7–4.5 m
IPCC SROCC	2300[a]	0.6–1.1 m	—	2.3–5.4 m
SROCC expert elicitation	2300[a]	0.5–2.3 m	—	2.0–5.4 m
Nauels et al. (2017)	2300[a]	0.8–1.4 m	1.3–2.3 m	3.4–6.8 m

Note. All projections are expressed relative to a baseline period of 1986–2005.
[a]Due to large uncertainties associated with post-2100 projections, these values are reported to the nearest 0.1 m.

Since the 21st century projections in both SROCC and the current study use AR5 methods with updates only for Antarctica, the GMSL-component projections at 2100 are identical to SROCC except for that term (Figures 8a–8c). For all three RCP scenarios our projections show substantially larger uncertainties in the Antarctica component with higher 95th percentiles that translate into more modest differences in GMSL. For the projections on extended time horizons, the methods differ to a greater extent. The SROCC 2300 projections are based on Table 13.8 of AR5 (Church et al., 2013), which drew upon a diverse set of model simulations that were broadly categorized as "Low," "Medium," and "High" scenarios. The extended 2300 projections presented here are based on the RCP scenarios, using a physical framework that is consistent with the 21st century projections and traceable to CMIP5 climate model simulations.

For 2300, we see substantial differences between SROCC and the present study for the available GMSL components (Figures 8d–8f). No estimate of post-2100 land water changes were made for AR5/SROCC, and our methods use a simple assumption of applying the 2100 rates over the period 2100–2300 (Table 1). The magnitude and relative importance of GMSL components at 2300 show strong scenario dependence. For RCP8.5 the dominant terms become thermal expansion, Greenland and Antarctica with the scenario-independent land water changes and mass-limited glacier contribution becoming less important compared to RCP2.6 or RCP4.5. RCP8.5 also shows the largest difference between the projected ranges for the present study and SROCC, with substantial differences for all three of the leading component terms.

The 5th to 95th percentile component ranges combine nonlinearly to the overall projected ranges for GMSL (Figure 8). The reason for this is illustrated in Figure 9, which shows the correlation between components evaluated across the 450,000-member Monte Carlo set at 2100. Global thermal expansion, Greenland surface mass balance, and worldwide glaciers are all positively correlated: Stronger warming promotes an increased contribution to GMSL from all of these terms.

Conversely, Antarctic surface mass balance is strongly anticorrelated with these terms because a warmer atmosphere tends to promote greater snowfall on Antarctica and reduce GMSL. As discussed in section 3.1, the AR5 methods resulted in a weak correlation between the surface mass balance and ice dynamics terms for Antarctica, which is also included here. We find similar correlations among components for all RCPs (Figure 9), although these tend to be slightly reduced for the higher emissions scenarios. Analysis of correlations at 2300 in the extended projections yields similar results (Figure S6), except for the glacier term that shows weaker correlations for RCP4.5 and RCP8.5 owing to the cap on total ice mass (illustrated in Figures 7e and 7f).

4.2. Local Sea-Level Projections

In this section we present our local MSL projections for 16 example tide gauge sites (Figure 1; Table S1). We focus our presentation on the highest (RCP8.5) and lowest (RCP2.6) emissions scenarios and include annual-mean tide gauge and satellite altimeter timeseries to illustrate the observed trends and local

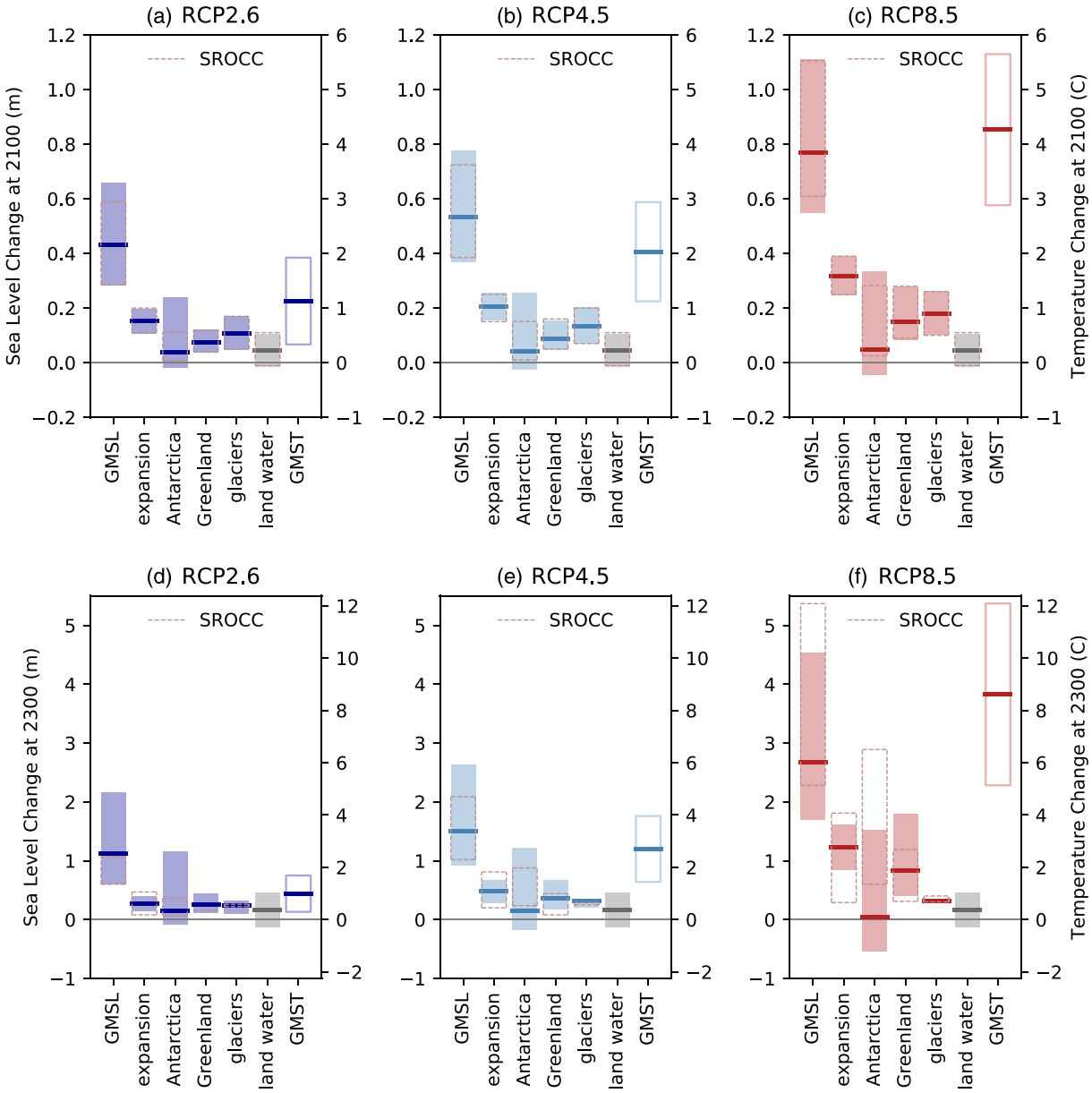

Figure 8. Components of projected global-mean sea-level (GMSL) change at 2100 (a–c, based on 21st century methods) and 2300 (d–f, based on extended 2300 methods) for RCP2.6 (left), RCP4.5 (middle), and RCP8.5 (right). The horizontal lines and shaded regions indicate the 50th percentile and the 5th to 95th percentile range, respectively, from the 450,000-member Monte Carlo simulation. Scenario-independent projections are shown in gray. For reference, the corresponding global-mean surface temperature (GMST) change is shown in the final column of each panel, with secondary *y*-axis on the right-hand side. All projections are expressed relative to the 1986–2005 average. Corresponding projected ranges from IPCC SROCC (Oppenheimer et al., 2019) are indicated by the dashed rectangles, based on the supplementary data files (GMSL and Antarctica) and table 13.SM.1/table 13.8 (other components) of Church et al. (2013).

sea-level variability (Figure 10). In general, there is good agreement between the observed decadal rates of MSL change and the early part of the projections, noting that the satellite altimeter timeseries do not account for vertical land motion processes associated with, for example, GIA, local subsidence, or tectonic activity. Locations of poorer agreement between observed and projected MSL trends include Lima and Port Louis. However, the high degree of consistency between altimeter and tide gauge observations at these locations suggests the discrepancy arises from climatic variability rather than non-GIA vertical land-motion processes. There is an apparent jump in the Pago Pago tide gauge timeseries towards the end of the record that could be related to a nearby earthquake in 2009 that resulted in several tsunami waves hitting the island. This jump is not seen in the satellite altimeter timeseries, confirming the likely role of substantial vertical

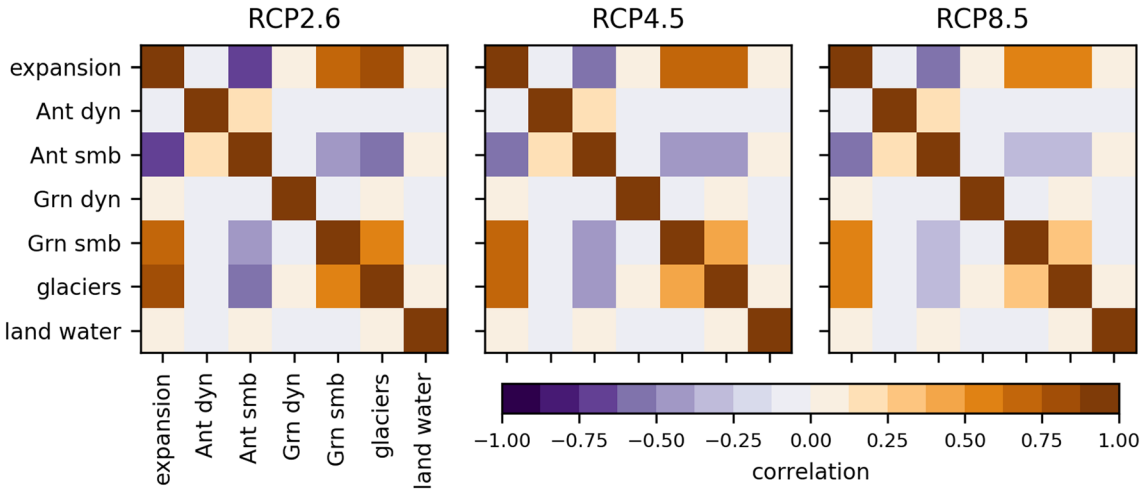

Figure 9. Correlation matrices of the different GMSL components for each RCP scenario based on the Monte Carlo spread at 2100. The matrices illustrate the relationships between GMSL components and explain why the total variance is not identical to the sum of the variances of the components.

land motion at this location. The observed interannual sea-level variability varies considerably by location and demonstrates that the reality of future sea-level change will be a combination of the climate response and unforced variability (e.g., Roberts et al., 2016).

As with GMSL, local MSL projections for the 21st century are similar to those reported in the IPCC SROCC (Figure 10) with agreement varying somewhat across tide gauge sites. Differences are thought to arise primarily from (i) the methods for estimating sterodynamic sea level and/or (ii) the methods used to combine sea-level components. It is apparent that the SROCC projections include some residual variability that originates from the underlying CMIP5 climate model simulations of sterodynamic sea-level change, which may also be present in the 1986–2005 reference state. Our regression-based approach to local sterodynamic sea-level change is designed to better isolate the climate change signal, resulting in smoother projections that do not include this simulated variability. This regression approach makes the approximation of a linear relationship between local sterodynamic sea-level change and global thermal expansion, which may also result in some differences with SROCC projections. Statistical approximations were used to combine the different local sea-level components for AR5 outside of the GMSL Monte Carlo framework that assumed terms were either perfectly correlated or perfectly uncorrelated, as described in equation 13.SM.1 of Church et al. (2013). This breaks the correlation structure among the GMSL components (Figure 9) and likely results in differences in the SROCC projected ranges for some locations. Re-running our local projections using only the GIA estimates used for AR5/SROCC (i.e., Lambeck and ICE5G, Figure 4) makes a negligible difference to the results shown in Figure 10. Analysis of the differences among our GRD fingerprints suggests that any differences in this regard are also likely to be negligible (see section 4.3).

Most tide gauge locations show that MSL is currently rising and that this rise will accelerate over the 21st century under the RCP8.5 scenario. The 21st century rates of sea-level change under RCP2.6 are relatively stable and most locations show the scenarios diverging from the mid-21st century. For most locations, the change in sea level over the 21st century is large compared to the tide gauge variability and implies that adaptation measures will be necessary to preserve current levels of coastal flood protection.

Barentsburg (Svalbard) and Reykjavik (Iceland) show atypical MSL projections. In both cases, the proximity to Greenland results in negative sea-level rise from this component (see Figure 3), which largely cancels out the positive contributions from the other climatic components, resulting in small scenario dependency at these locations. Barentsburg has a substantial rate of MSL fall associated with GIA, which accounts for the more negative values seen at this location compared to Reykjavik. While Oslo retains substantive scenario dependency, the negative GIA signal results in a much-reduced rates of rise under RCP8.5 and the expectation of a sea-level fall under RCP2.6. Barentsburg, Reykjavik, and Oslo clearly illustrate that projections of GMSL cannot necessarily be taken as indicative of local MSL change.

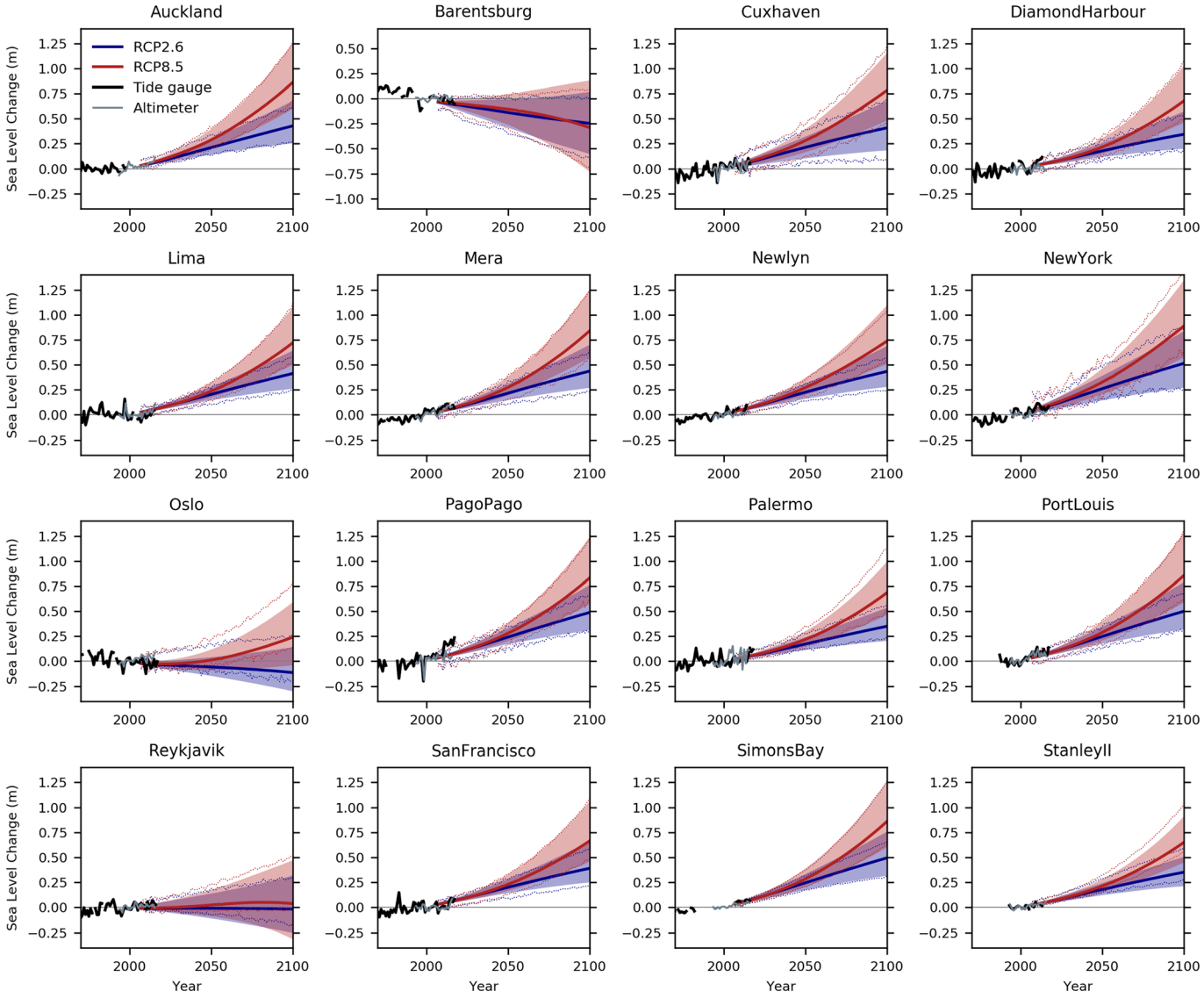

Figure 10. Local sea-level projections for RCP2.6 (blue) and RCP8.5 (red). Shaded regions indicate the 5th to 95th percentile range of the 100,000-member Monte Carlo simulation. The dotted lines indicate the 5th and 95th percentile projections from the IPCC SROCC (Oppenheimer et al., 2019). Local annual-mean tide gauge data are indicated by the solid black line. Local annual-mean satellite altimeter data are indicated by the solid gray line. All timeseries are shown relative to the 1986–2005 average. Note the different *y*-axis for Barentsburg.

Excluding these atypical tide gauge locations, we still see substantive variations in future sea-level rise across the remaining tide gauge sites. The range of behavior is spanned by New York and Stanley II with ranges at 2100 under RCP2.6 (RCP8.5) of 0.27–0.84 m (0.57–1.35 m) and 0.21–0.51 m (0.45–0.91 m), respectively. New York has a large spread in sterodynamic sea-level change and also a substantial positive contribution from GIA. The relative proximity of Stanley II (the Falkland Islands) to Antarctica results in a strong attenuation of the MSL change associated with Antarctic ice dynamics, which reduces both the overall magnitude and the spread of uncertainty in future projections.

We combine the tide gauge data with our local MSL projections to explore the relative importance of variability, scenario, and model uncertainty over the 21st century following Hawkins and Sutton (2009). Local sea-level variability is estimated by de-trending the tide gauge records and computing the standard deviation of the residual timeseries. The scenario standard deviation is estimated using the central estimates under RCP2.6, RCP4.5, and RCP8.5. Finally, the model uncertainty is estimated by computing the average standard deviation of the Monte Carlo simulation across the three RCP scenarios. Our analysis suggests that sea-level

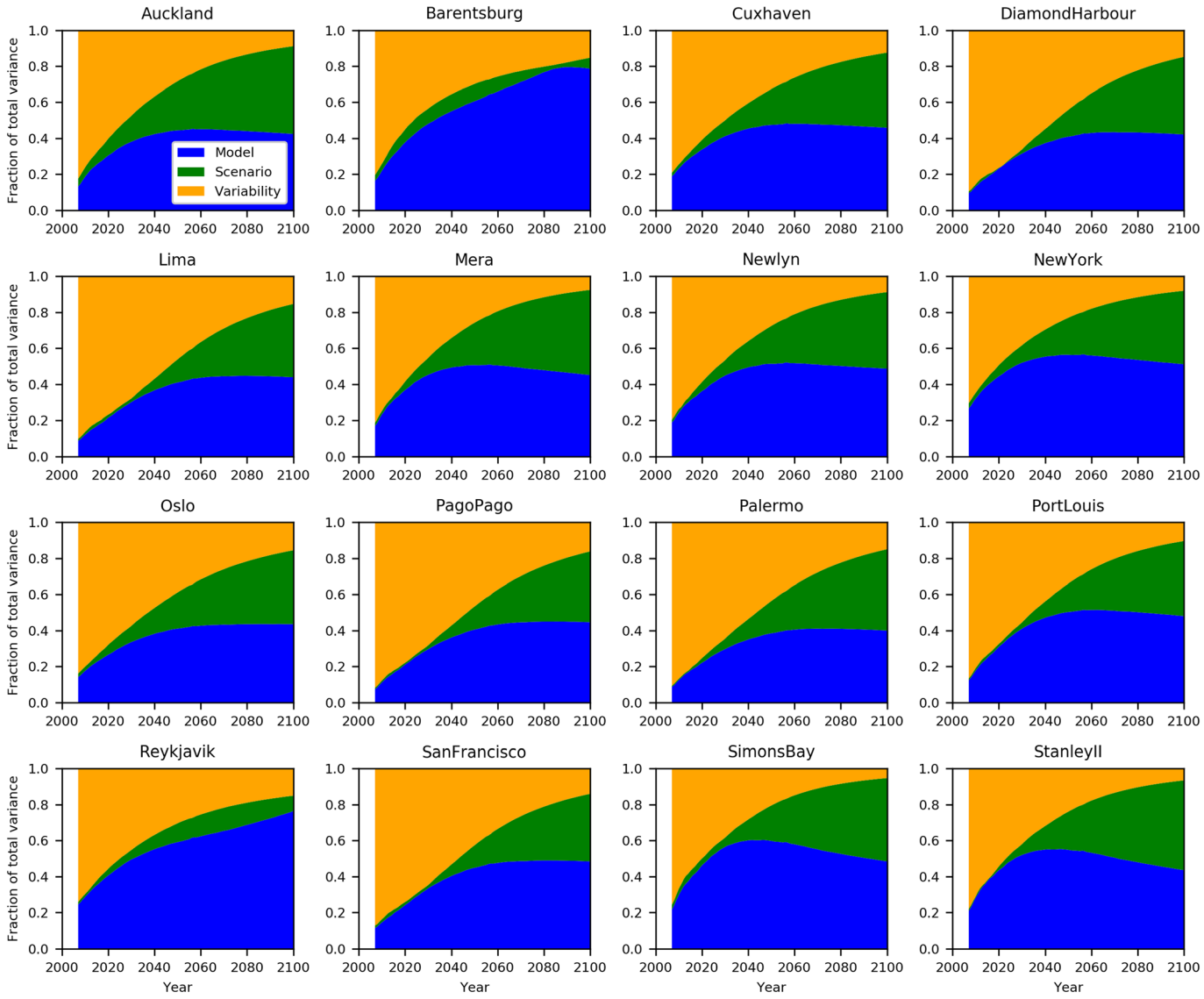

Figure 11. Assessment of the fraction of total variance of sea-level change explained by model, scenario, and variability, following Hawkins and Sutton (2009) as indicated in the figure legend for Auckland.

variability is likely to be a key driver of MSL change for the coming decades at all tide gauge locations (Figure 11). Conversely, the impact of RCP scenario will only make a substantive contribution towards the end of the 21st century. At Barentsburg and Reykjavik, differences across scenarios explain 10–20% of the projected variance, which is related to the negative contribution from Greenland canceling out other terms (as discussed above). At all locations, model uncertainty explains a large share of the overall variance and is particularly important for Barentsburg and Reykjavik.

The extended 2300 projections again illustrate the large levels of committed sea-level change associated with both RCP2.6 and RCP8.5 for the coming centuries (Figure 12). The projections show greater separation between these two scenarios post-2100 and the large degree of uncertainty on these time horizons. For several sites, the projected range at 2300 for RCP8.5 exceeds 5 m. Even under RCP2.6 central estimates of sea-level rise are in excess of 1 m for most locations, and the projected range exceeds 2 m at many locations. The geographical variations in projections seen over the 21st century (Figure 10) are essentially preserved (as a proportion of the signal size), resulting in differences in the projected ranges up to several meters. At these extended time horizons, the projected sea-level changes are an order of magnitude greater than the interannual tide gauge variability. At most locations, the magnitude of MSL rise and the projected range is larger than

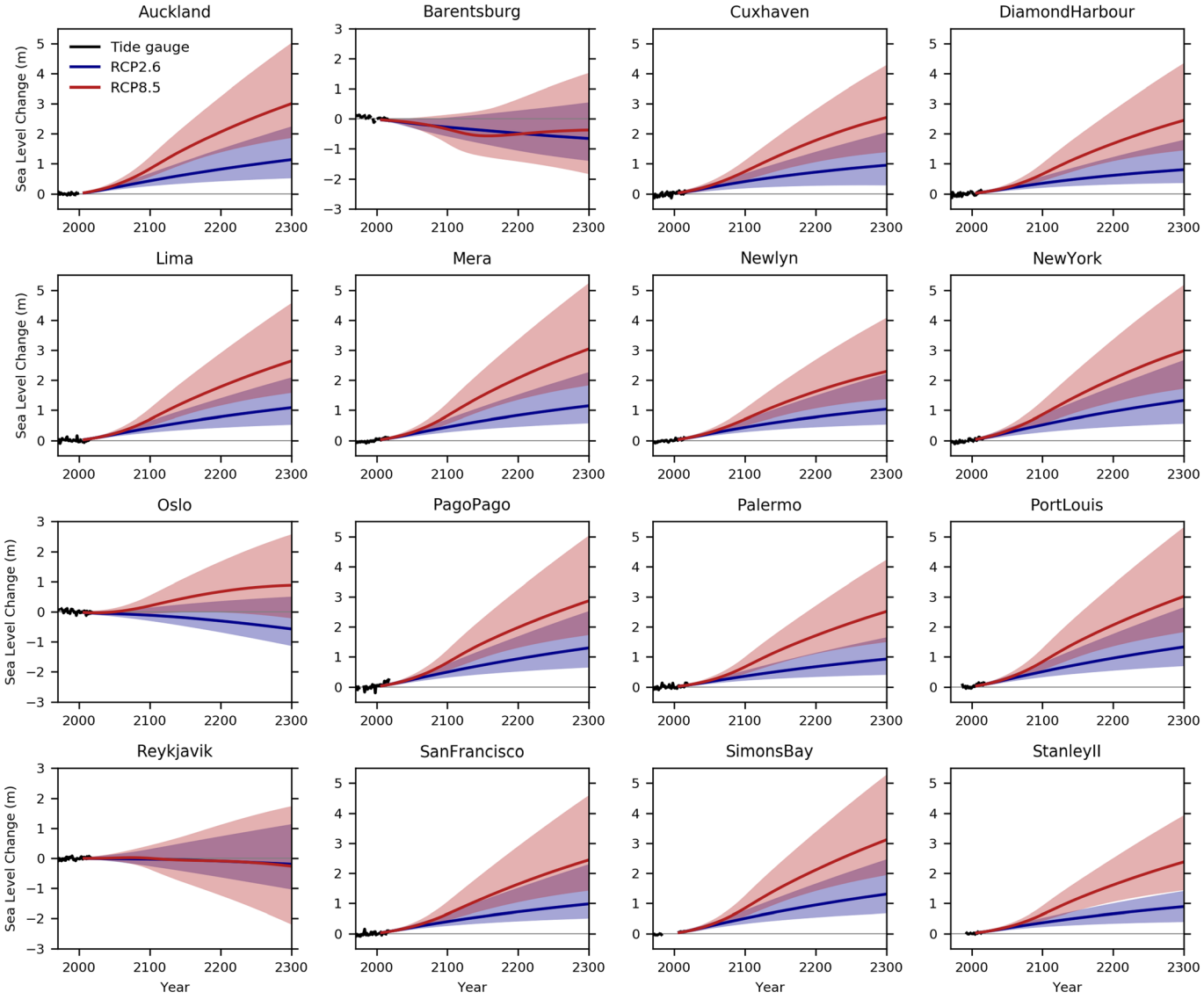

Figure 12. Local sea-level projections for RCP2.6 (blue) and RCP8.5 (red). Shaded regions indicate the 5th to 95th percentile range of the 100,000-member Monte Carlo simulation. Annual tide gauge data are indicated by the black line. All timeseries are shown relative to the 1986–2005 average. Note the different *y*-axis for Barentsburg, Oslo, and Reykjavik.

for the corresponding projection of GMSL (Figure 7). A large part of the increased spread comes from the amplification of the Antarctic ice sheet signals (the greatest source of uncertainty, Figure 8) by the GRD patterns, which have local values greater than unity for most tide gauge sites.

4.3. Analysis of Model Uncertainty

In this section, we further explore the contributions to the model uncertainty that is represented by the projected ranges of sea-level change for a given scenario. In particular, we consider which MSL components are dominant in determining the total variance in projected ranges as a function of geographic location, time horizon, and RCP scenario. We compute the total variance for the GMSL timeseries and several example tide gauge locations for both RCP2.6 and RCP8.5. We also compute the covariance matrix across the Monte Carlo ensembles as a function of time. The off-diagonal elements of the matrix are combined into an additional term that we label "interactions"—with this contribution arising from correlations among the components. While this analysis was performed on both, the 21st century and extended 2300 projections, the results up to 2100 are similar (Figure S7). For this reason, we focus our presentation on the extended 2300 results so that we can look across all relevant time scales. In some instances, the anticorrelation between terms leads to a

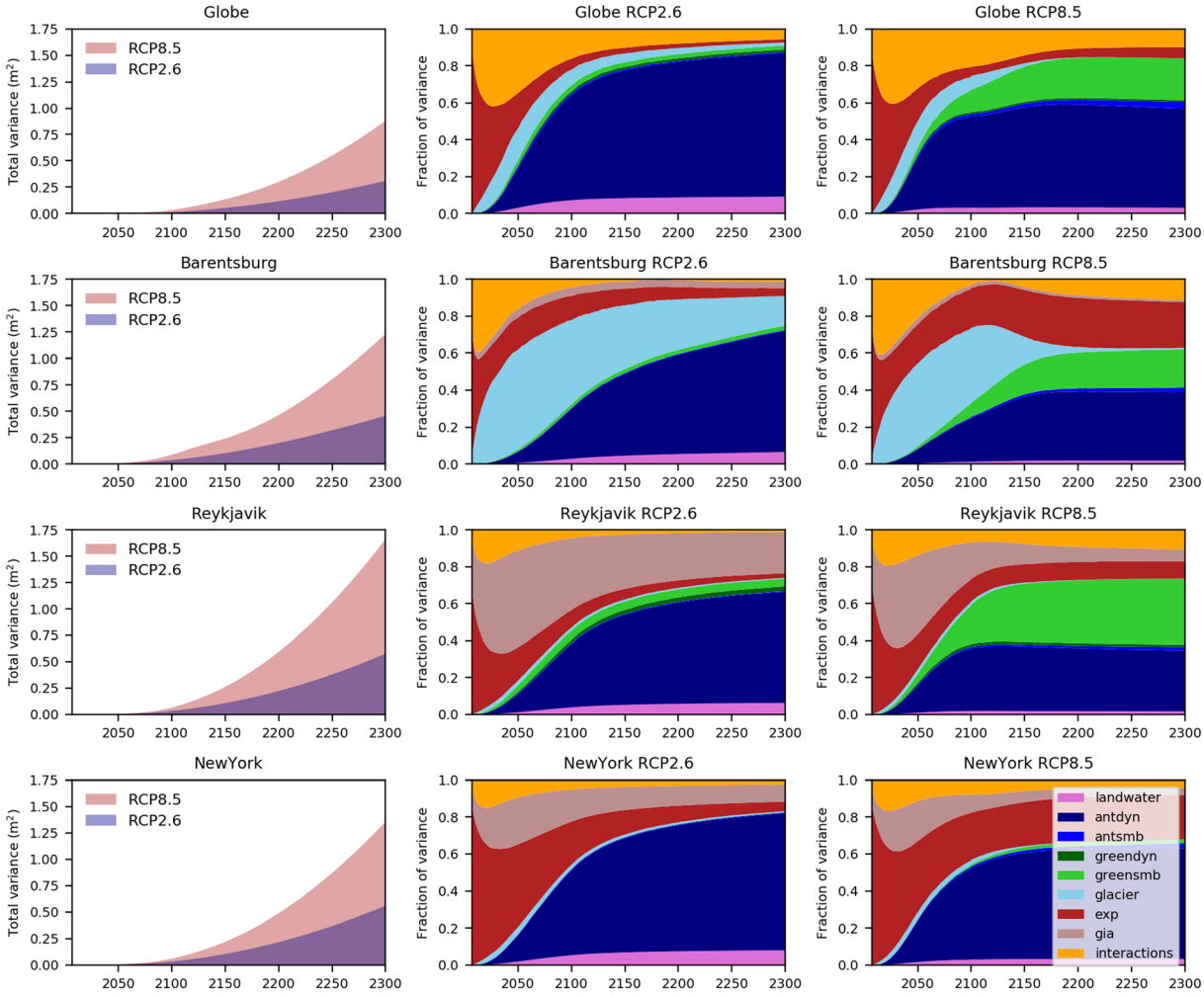

Figure 13. Time evolution of variance associated with model uncertainty for GMSL and three example tide gauge sites under RCP2.6 and RCP8.5 based on the extended projections to 2300. The left column shows the time evolution of total variance. The central and right columns show the time-evolution fraction of variance explained for RCP2.6 and RCP8.5, respectively, as indicated in the bottom-right panel legend. For GMSL, "exp" refers to global thermal expansion. For tide gauge sites, "exp" refers to sterodynamic sea-level change. Estimates for each variance term come from the diagonal of the covariance matrix. The off-diagonal contributions are presented as a combined term labeled "interactions."

reduction of total variance. For simplicity of the graphical representation and to focus discussion on the relative importance of contributions to variance in general, our analysis is based on the absolute variances.

The total variance at 2300 under RCP8.5 is more than double that for RCP2.6, both globally and at all tide gauge locations (Figures 13 and 14; left column), indicating the inherently larger uncertainties under high emissions scenarios, related to the uncertainty in model climate sensitivity. For GMSL (Figure 13, top row) the ensemble spread is initially dominated by global thermal expansion, but uncertainty in Antarctic ice dynamics becomes the dominant term from the latter half of the 21st century. Prior to 2100, there is little difference in the breakdown of variance by RCP scenario. Post-2100 we see a much larger contribution from Greenland surface mass balance under RCP8.5, becoming the second largest source of variance after Antarctic ice dynamics.

The breakdown of variance for Barentsburg (Svalbard; Figure 13) shows a dominant contribution from glaciers over the 21st century, and this term remains important out to 2300. This feature is due to the large glacier mass on Svalbard, which leads to large negative values in the GRD estimates associated primarily with vertical land uplift. We see strong scenario dependence on the contributions to variance post-2100, with Greenland surface mass balance and sterodynamic sea-level change becoming much more important under RCP8.5 than RCP2.6. Variance arising from GIA estimates makes only a minor contribution at this location.

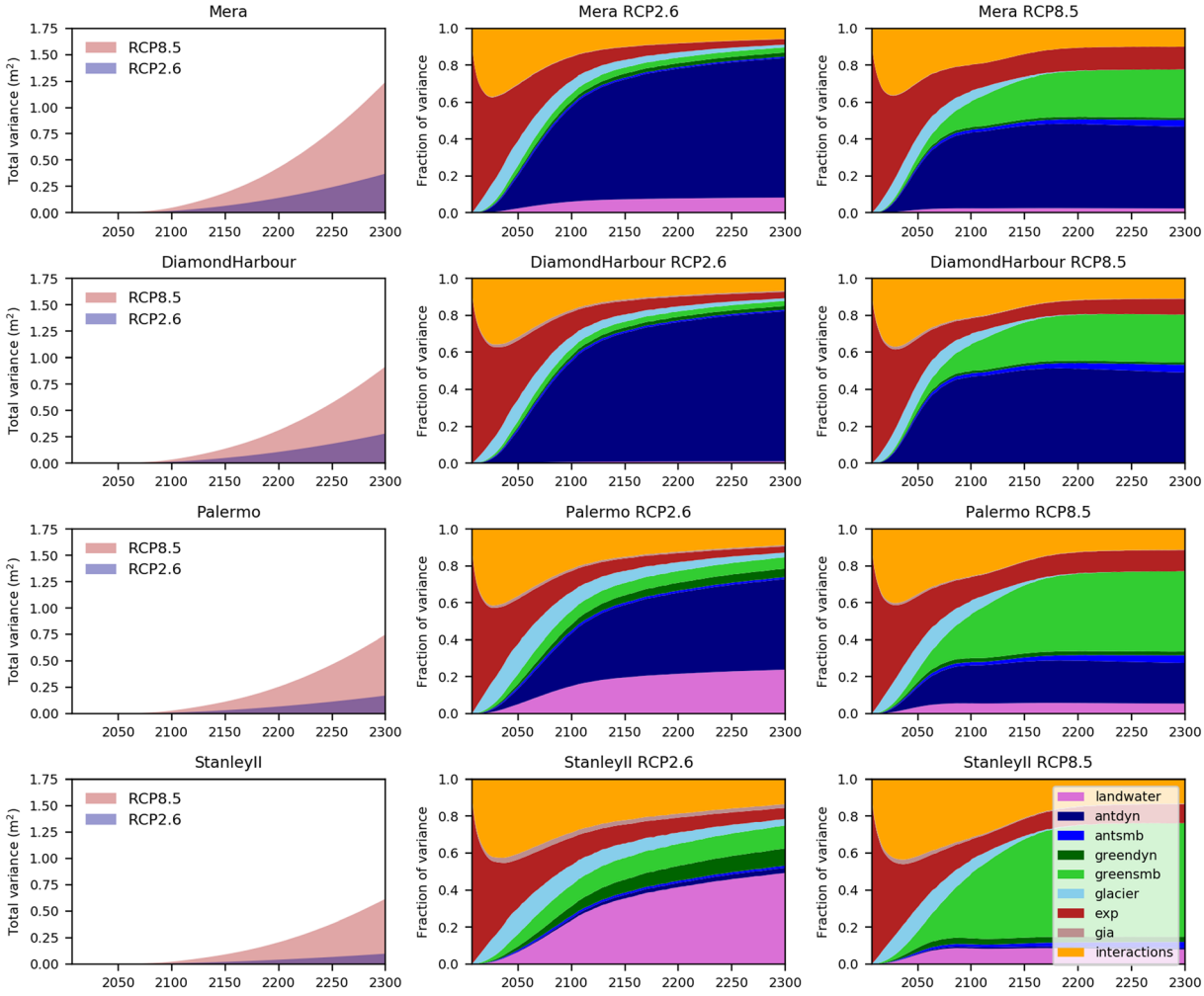

Figure 14. Time evolution of variance associated with model uncertainty for four example tide gauge sites under RCP2.6 and RCP8.5 based on the extended projections to 2300. The left column shows the time evolution of total variance. The central and right columns show the time-evolution fraction of variance explained for RCP2.6 and RCP8.5, respectively, as indicated in the bottom-right panel legend. Note that "exp" refers to sterodynamic sea-level change. Estimates for each variance term come from the diagonal of the covariance matrix. The off-diagonal contributions are presented as a combined term labeled "interactions."

In contrast, Reykjavik (Iceland; Figure 13) has a large contribution to variance from the different GIA estimates, and this is the dominant source of variance over most of the 21st century. Post-2100, Antarctic ice dynamics dominates the variance under RCP2.6, with GIA remaining an important contribution for this scenario. For RCP8.5, Greenland surface mass balance and Antarctic ice dynamics contribute similarly to total variance post-2100.

As discussed in the previous section, New York (USA; Figure 13) has a particularly large uncertainty associated with future changes in ocean circulation, and this is reflected in the dominance of sterodynamic sea-level change over the 21st century. GIA is also relatively important at this location, particularly under RCP2.6. Again, it is ultimately the Antarctic ice dynamics that becomes the dominant source of variance post-2100, but sterodynamic sea-level change remains a sizeable contribution under RCP8.5.

The breakdown of variance for Mera (Japan; Figure 14) and Diamond Harbour (India; Figure 14) is typical of many lower latitude locations with characteristics that are very similar to that of GMSL (Figure 13, top row). Mera has a substantive contribution from land water under RCP2.6 that is absent from Diamond Harbour. At both locations, the contribution from GIA is very small, indicating that future changes will be dominated by contemporary climate-driven changes. As with all tide gauge locations, we cannot rule out the potential importance of nonclimatic processes, particularly those associated with vertical motion (e.g., subsidence and tectonic activity).

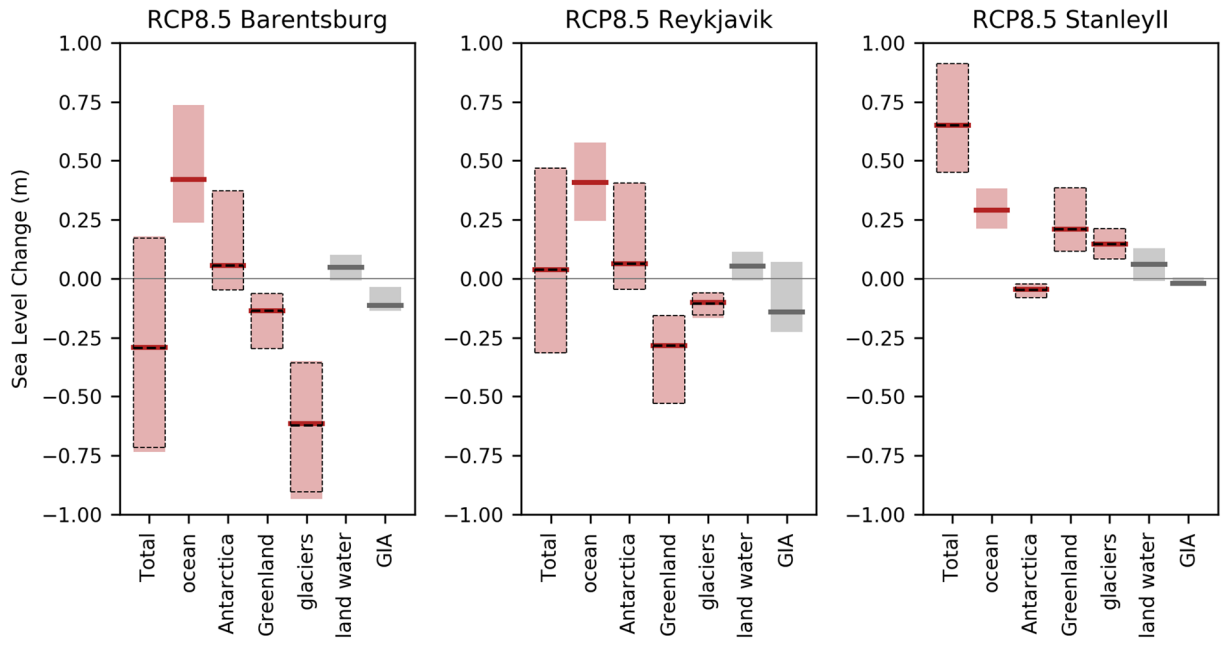

Figure 15. Projected ranges of MSL change at 2100 for three example tide gauge locations under RCP8.5. The dashed lines indicate the results when the average of three GRD estimates (rather than random selection) is used in the Monte Carlo simulations. All projections are expressed relative to a baseline period of 1986–2005. Scenario-independent components are indicated in gray.

Palermo (Argentina; Figure 14) shows a marked reduction in the contribution from Antarctic ice dynamics, which is associated with its proximity to West Antarctica (Figure 3b). This is also reflected in the reduced total variance seen at this tide gauge location for both RCP scenarios compared to GMSL. This results in a larger relative importance of many of the other MSL components. Variance arising from different scenarios of land water change is the second largest post-2100 term (after Antarctic ice dynamics) under RCP2.6. For RCP8.5, post-2100 variance is dominated by Greenland surface mass balance.

Like Palermo, Stanley II (Falkland Islands; Figure 14) also sees a reduced total variance compared to GMSL resulting from the proximity of Antarctica. In this case, Antarctic ice dynamics makes a negligible contribution to total variance because the tide gauge location is close to the zero contour of the associated GRD pattern of MSL change (Figure 3b). The relative importance of the other terms over the 21st century is similar to Palermo. Post-2100, land water dominates the variance under the RCP2.6 scenario, and Greenland surface mass balance dominates for the RCP8.5 scenario. In the absence of substantive signals from Antarctic ice dynamics, the anticorrelated contributions of Greenland and Antarctic surface mass balance lead to a particularly large "interactions" term that reduces the overall variance compared to GMSL.

The importance of the land water contribution for both Palermo and Stanley II under RCP2.6 arises for a number of reasons. First, the land water projections are scenario-independent, so its relative importance increases under RCP2.6 compared to RCP8.5. Second, the relative importance of land water is further increased at these locations due to the strong attenuation of the Antarctica signals, in relation to GRD (Figure 3), as discussed above. Third, both Palermo and Stanley II are in a region where the global land water contribution (and its uncertainty) is amplified at regional scales by the GRD patterns (Figure 3).

Overall, we see a strong geographic and time dependence of the contribution to total variance. There is little scenario dependence until after 2100, and this is typified by a substantially increased contribution from Greenland surface mass balance under RCP8.5. Antarctic ice dynamics tend to dominate the total variance from the latter half of the 21st century out to 2300 under both RCP2.6 and RCP8.5. However, this is not the case for locations in proximity to West Antarctica (e.g., southern South America), where the GRD pattern of MSL results in greatly attenuated signals for Antarctic ice dynamics. The contrasting results presented here make a clear case for the need for site-specific local sea-level projections. In addition, the reduction of

variance (uncertainty) in future projections implies different research priorities, depending on geographic location and time horizon.

As part of our analysis of variance, we also investigate the contribution from uncertainty in the GRD estimates presented in section 2.4 (Figure 3). We choose the three tide gauge sites with the largest spread in one or more GRD components, that is, Barentsburg, Reykjavik, and Stanley II, and conduct the following simple analysis. We run an additional instance of the MSL Monte Carlo for each location using the average value of the GRD fingerprints at each site for RCP8.5 (i.e., the scenario with the largest signal). The projected MSL and component ranges are then compared to the full Monte Carlo simulations that include a random choice of GRD estimate. The results demonstrate that using multiple GRD estimates has an essentially negligible contribution to the total variance—the differences at 2100 for RCP8.5 are just about perceptible for Barentsburg (Figure 15). It is therefore reasonable to use only a single set of GRD estimates when computing local MSL projections. However, our analysis does not account for uncertainty in the associated space-time mass distributions that is used to compute the GRD patterns. This is an area that may benefit from further research.

5. Summary and Conclusions

We have presented MSL projections under the RCP2.6, RCP4.5, and RCP8.5 climate change scenarios for both global-mean sea level and for a number of example tide gauge locations around the world. Our 21st century projections are directly traceable to the CMIP5-based sea-level projections presented in AR5 (Church et al., 2013) with updated treatment of the contribution from Antarctic ice dynamics following Levermann et al. (2014) and show similar results to projections presented in the SROCC (Oppenheimer et al., 2019). Our regression approach for sterodynamic sea-level change more cleanly isolates the forced signal and enables us to characterize the relative importance of variance arising from scenario, model spread, and observed sea-level variability over the 21st century, following Hawkins and Sutton (2009). A key aspect of the study is the use of the same Monte Carlo framework for both global and local sea-level projections. This means that global and local projections are entirely consistent, preserving the correlations among components and allowing us to quantify the contributions to total variance (uncertainty) by geographic location, time horizon, and scenario. We introduced a new set of exploratory extended projections to 2300 that are rooted in CMIP5 projections through the use of a physically based emulator to extend individual CMIP5 climate model simulations (Palmer, Harris, et al., 2018). These emulator-based projections are designed for maximum consistency with the 21st century projections and show a high level of agreement at 2100. Our main findings are summarized as follows:

1. We have developed a consistent set of local sea-level projections that are directly traceable to the GMSL projections developed for AR5 and preserve the relationships between components (an important factor in determining the fraction of variance explained).
2. Our projections of GMSL at both 2100 and 2300 yield similar numbers to those recently reported in the IPCC Special Report on the Ocean and Cryosphere in a Changing Climate (IPCC, 2019), noting the large inherent uncertainties associated with multicentury time horizons. For RCP2.6, our projected ranges at 2300 are larger than some recent studies (including the SROCC likely range) and may have important implications for long-term adaptation planning.
3. Combined analysis of local MSL projections and tide gauge records suggests that sea-level variability dominates the total variance in the coming decades, with climate change scenario becoming increasingly important over the 21st century. Model uncertainty tends to be the largest source of variance from the mid-21st century.
4. Local MSL projections can show large departures from the GMSL response and are typically associated with substantially larger uncertainties. A few locations will see MSL decrease in future owing to spatial patterns of GRD and the local contribution from GIA.
5. On century time scales, the projected MSL changes are large compared to observations of local sea-level variability. This indicates that many places will be exposed to greater coastal flood risk unless effective adaptation measures are taken.
6. The extended projections to 2300 illustrate the large degree of committed sea-level rise even in strong mitigation scenarios. They also illustrate the substantially increased risk for the highest emissions scenarios, which are associated with several meters of MSL rise at most tide gauge locations.

7. Correlations between component terms mean that the variance of the total MSL change is not identical to the sum of the variances of the components. Moreover, the breakdown of variance depends on both, geographic location and time horizon, with differences in scenario post-2100. Antarctic ice dynamics dominate the total variance post-2100 except at locations where GRD patterns strongly attenuate this signal.
8. This study highlights the need for development of site-specific MSL projections for effective planning (GMSL projections of cannot be reliably used to indicate the local changes). The time-space-scenario dependence in the contributions to total variance suggests that research priorities for reducing uncertainty in sea-level projections are likely to vary by geographic location and planning time horizon.

Data Availability Statement

The data for the original sea-level projections included in this work will be made available through the U.K. Centre for Environmental Data Analysis (CEDA) Archive https://www.ceda.ac.uk/services/ceda-archive/.

Acknowledgments

M. P., J. G., D. C., T. H., J. L., and C. R. were supported by the Met Office Hadley Centre Climate Programme funded by the BEIS and Defra. M. B. was funded by the German climate modeling project PalMod (FKZ: 01LP1502E) supported by the German Federal Ministry of Education and Research (BMBF) as a Research for Sustainability initiative (FONA). V. K. and PalMod (FKZ:01LP1502E and FKZ:01LP1503A) as well as to the Helmholtz project, "Advanced Earth System Modelling Capacity (ESM)." G. S. was funded by an FFABR (Finanziamento delle Attività Base di Ricerca) grant of the MIUR (Ministero dell'Istruzione, dell'Università e della Ricerca) and by a DiSPeA (Dipartimento di Scienze Pure e Applicate of the Urbino University) research grant. We acknowledge the World Climate Research Programme's Working Group on Coupled Modelling, which is responsible for CMIP, and we thank the climate modeling groups (listed in Table S2) for producing and making available their model output. For CMIP the U.S. Department of Energy's Program for Climate Model Diagnosis and Intercomparison provides coordinating support and led development of software infrastructure in partnership with the Global Organization for Earth System Science Portals. We would like to thank two anonymous reviewers for providing constructive comments on an earlier version of this paper.

References

Argus, D. F., Peltier, W. R., Drummond, R., & Moore, A. W. (2014). The Antarctica component of postglacial rebound model ICE-6G_C (VM5a) based upon GPS positioning, exposure age dating of ice thicknesses, and relative sea level histories. *Geophysical Journal International*, *198*(1), 537–563. https://doi.org/10.1093/gji/ggu140

Bamber, J., & Aspinall, W. (2013). An expert judgement assessment of future sea level rise from the ice sheets. *Nature Clim Change*, *3*, 424–427. https://doi.org/10.1038/nclimate1778

Bilbao, R. A. F., Gregory, J. M., & Bouttes, N. (2015). Analysis of the regional pattern of sea level change due to ocean dynamics and density change for 1993–2099 in observations and CMIP5 AOGCMs. *Climate Dynamics*, *45*, 2647–2666. https://doi.org/10.1007/s00382-015-2499-z

Bouttes, N., Gregory, J. M., Kuhlbrodt, T., & Smith, R. S. (2014). The drivers of projected North Atlantic sea level change. *Climate Dynamics*, *43*, 1531–1544. https://doi.org/10.1007/s00382-013-1973-8

Cannaby, H., Palmer, M. D., Howard, T., Bricheno, L., Calvert, D., Krijnen, J., et al. (2016). Projected sea level rise and changes in extreme storm surge and wave events during the 21st century in the region of Singapore. *Ocean Science*, *12*, 613–632. https://doi.org/10.5194/os-12-613-2016

Church, J. A., Clark, P. U., Cazenave, A., Gregory, J. M., Jevrejeva, S., Levermann, A., et al. (2013). Sea level change. In T. F. Stocker, et al. (Eds.), *Climate change 2013: The physical science basis* (pp. 1137–1216). Cambridge, UK and New York, NY: Cambridge University Press.

DeConto, R. M., & Pollard, D. (2016). Contribution of Antarctica to past and future sea-level rise. *Nature*, *531*, 591. https://doi.org/10.1038/nature17145

Edwards, T. L., Brandon, M. A., Durand, G., Edwards, N. R., Golledge, N. R., Holden, P. B., et al. (2019). Revisiting Antarctic ice loss due to marine ice-cliff instability. *Nature*, *566*(7742), 58–64. https://doi.org/10.1038/s41586-019-0901-4

Farinotti, D., Huss, M., Fürst, J. J., Landmann, J., Machguth, H., Maussion, F., & Pandit, A. (2019). A consensus estimate for the ice thickness distribution of all glaciers on Earth. *Nature Geoscience*, *12*, 168–173. https://doi.org/10.1038/s41561-019-0300-3

Fettweis, X., Franco, B., Tedesco, M., van Angelen, J. H., Lenaerts, J. T. M., van den Broeke, M. R., & Gallée, H. (2013). Estimating the Greenland ice sheet surface mass balance contribution to future sea level rise using the regional atmospheric climate model MAR. *The Cryosphere*, *7*, 469–489. https://doi.org/10.5194/tc-7-469-2013

Garner, A. J., Weiss, J. L., Parris, A., Kopp, R. E., Horton, R. M., Overpeck, J. T., & Horton, B. P. (2018). Evolution of 21st century sea level rise projections. *Earth's Future*, *6*, 1603–1615. https://doi.org/10.1029/2018EF000991

Geoffroy, O., Saint-Martin, D., Olivié, D. J., Voldoire, A., Bellon, G., & Tytéca, S. (2013). Transient climate response in a two-layer energy-balance model. Part I: Analytical solution and parameter calibration using CMIP5 AOGCM experiments. *Journal of Climate*, *26*, 1841–1857. https://doi.org/10.1175/JCLI-D-12-00195.1

Good, P., Gregory, J. M., Lowe, J. A., & Andrews, T. (2013). Abrupt CO_2 experiments as tools for predicting and understanding CMIP5 representative concentration pathway projections. *Climate Dynamics*, *40*, 1041–1053. https://doi.org/10.1007/s00382-012-1410-4

Gregory, J. M., Bouttes-Mauhourat, N., Griffies, S. M., Haak, H., Hurlin, W. J., Jungclaus, J., et al. (2016). The Flux-Anomaly-Forced Model Intercomparison Project (FAFMIP) contribution to CMIP6: Investigation of sea-level and ocean climate change in response to CO_2 forcing. *Geoscientific Model Development*, *9*, 3993–4017. https://doi.org/10.5194/gmd-9-3993-2016

Gregory, J. M., Griffies, S. M., Hughes, C. W., Lowe, J. A., Church, J. A., Fukumori, I., et al. (2019). Concepts and terminology for sea level: Mean, variability and change, both local and global. *Surveys in Geophysics*. https://doi.org/10.1007/s10712-019-09525-z

Grinsted, A. (2013). An estimate of global glacier volume. *The Cryosphere*, *7*, 141–151. https://doi.org/10.5194/tc-7-141-2013

Hawkins, E., & Sutton, R. (2009). The potential to narrow uncertainty in regional climate predictions. *Bulletin of the American Meteorological Society*, *90*, 1095–1108. https://doi.org/10.1175/2009BAMS2607.1

Hinkel, J., Church, J. A., Gregory, J. M., Lambert, E., le Cozannet, G., Lowe, J., et al. (2019). Meeting user needs for sea level rise information: A decision analysis perspective. *Earth's Future*, *7*, 320–337. https://doi.org/10.1029/2018EF001071

Hobbs, W., Palmer, M. D., & Monselesan, D. (2016). An energy conservation analysis of ocean drift in the CMIP5 global coupled models. *Journal of Climate*, *29*, 1639–1653. https://doi.org/10.1175/JCLI-D-15-0477.1

Hock, R., Marzeion, B., Bliss, A., Giesen, R., Hirabayashi, Y., Huss, M., et al. (2019). GlacierMIP—A model intercomparison of global-scale glacier mass-balance models and projections. *Journal of Glaciology*, *65*(251), 453–467, https://doi.org/10.1017/jog.2019.22

Holgate, S. J., Matthews, A., Woodworth, P. L., Rickards, L. J., Tamisiea, M. E., Bradshaw, E., et al. (2013). New data systems and products at the permanent service for mean sea level. *Journal of Coastal Research*, *29*(3), 493–504. https://doi.org/10.2112/JCOASTRES-D-12-00175.1

Howard, T., Palmer, M. D., & Bricheno, L. M. (2019). Contributions to 21st century projections of extreme sea-level change around the UK. *Environmental Research Communications*, *1*(9), 95002. https://doi.org/10.1088/2515-7620/ab42d7

IPCC (2019). Summary for policymakers. In H.-O. Pörtner, et al. (Eds.), *IPCC Special Report on the Ocean and Cryosphere in a Changing Climate*. https://www.ipcc.ch/srocc/cite-report/

Jackson, L. P., & Jevrejeva, S. (2016). A probabilistic approach to 21st century regional sea-level projections using RCP and high-end scenarios. *Global and Planetary Change*, *146*, 179–189. https://doi.org/10.1016/j.gloplacha.2016.10.006

Jevrejeva, S., Frederikse, T., Kopp, R. E., le Cozannet, G., Jackson, L. P., & van de Wal, R. S. W. (2019). Probabilistic sea level projections at the coast by 2100. *Surveys in Geophysics*, *40*, 1673–1696. https://doi.org/10.1007/s10712-019-09550-y

Klemann, V., & Groh, A. (2013). Practical: Ice and loading. In A. Eicker, J. Kusche (Eds.), *Lecture notes from the summer school of DFG SPP1257 global water cycle* (Schriftenreihe Institut für Geodäsie und Geoinformation 30, pp. 227–236). Universität Bonn, Institut für Geodäsie und Geoinformation.

Kopp, R. E., Horton, R. M., Little, C. M., Mitrovica, J. X., Oppenheimer, M., Rasmussen, D. J., et al. (2014). Probabilistic 21st and 22nd century sea-level projections at a global network of tide-gauge sites. *Earth's Future*, *2*, 383–406. https://doi.org/10.1002/2014EF000239

Legeais, J.-F., Ablain, M., Zawadzki, L., Zuo, H., Johannessen, J. A., Scharffenberg, M. G., et al. (2018). An improved and homogeneous altimeter sea level record from the ESA Climate Change Initiative. *Earth System Science Data*, *10*, 281–301. https://doi.org/10.5194/essd-10-281-2018

Levermann, A., Winkelmann, R., Nowicki, S., Fastook, J. L., Frieler, K., Greve, R., et al. (2014). Projecting Antarctic ice discharge using response functions from SeaRISE ice-sheet models. *Earth Surface Dynamics*, *5*, 271–293. https://doi.org/10.5194/esd-5-271-2014

Lorbacher, K., Nauels, A., & Meinhausen, M. (2015). Complementing thermosteric sea level rise estimates. *Geoscientific Model Development*, *8*, 2723–2734. https://doi.org/10.5194/gmd-8-2723-20

Lowe, J. A., Bernie, D., Bett, P., Bricheno, L., Brown, S., Calvert, D., et al. (2018). *UKCP18 science overview report* (pp. 1–73). Available from https://www.metoffice.gov.uk/pub/data/weather/uk/ukcp18/science-reports/UKCP18-Overview-report.pdf

Martinec, Z., & Hagedoorn, J. (2014). The rotational feedback on linear-momentum balance in glacial isostatic adjustment. *Geophysical Journal International*, *199*, 1823–1846. https://doi.org/10.1093/gji/ggu369

Martinec, Z., Klemann, V., van der Wal, W., Riva, R. E. M., Spada, G., Sun, Y., et al. (2018). A benchmark study of numerical implementations of the sea-level equation in GIA modelling. *Geophysical Journal International*, *215*(1), 389–414. https://doi.org/10.1093/gji/ggy280

Meinshausen, M., Smith, S. J., Calvin, K., Daniel, J. S., Kainuma, M., Lamarque, J.-f., et al. (2011). The RCP greenhouse gas concentrations and their extension from 1765 to 2300. *Climatic Change*, *109*, 213. https://doi.org/10.1007/s10584-011-0156-z

Nakada, M., & Lambeck, K. (1988). The melting history of the late Pleistocene Antarctic ice sheet. *Nature*, *333*(6168), 36–40. https://doi.org/10.1038/333036a0

Nauels, A., Meinshausen, M., Mengel, M., Lorbacher, K., & Wigley, T. M. L. (2017). Synthesizing long-term sea level rise projections—The MAGICC sea level model v2.0. *Geoscientific Model Development*, *10*, 2495–2524. https://doi.org/10.5194/gmd-10-2495-2017

Nerem, R. S., Beckley, B. D., Fasullo, J. T., Hamlington, B. D., Masters, D., & Mitchum, G. T. (2018). Climate-change–driven accelerated sea-level rise. *Proceedings of the National Academy of Sciences*, *115*(9), 2022–2025. https://doi.org/10.1073/pnas.1717312115

Oppenheimer, M., Glavovic, B. C., Hinkel, J., van de Wal, R., Magnan, A. K., Abd-Elgawad, A., et al. (2019). Sea level rise and implications for low-lying islands, coasts and communities. In H.-O. Pörtner et al. (Eds.), *IPCC Special Report on the Ocean and Cryosphere in a Changing Climate*.

Palmer, M. D., Harris, G. R., & Gregory, J. M. (2018). Extending CMIP5 projections of global mean temperature change and sea level rise due to thermal expansion using a physically-based emulator. *Environmental Research Letters*, *13*(8), 84003.

Palmer, M. D., Howard, T., Tinker, J., Lowe, J., Bricheno, L., Calvert, D., et al. (2018). UKCP18 marine report, 133 pp. Available from https://www.metoffice.gov.uk/pub/data/weather/uk/ukcp18/science-reports/UKCP18-Marine-report.pdf

Peltier, W. R. (2004). Global glacial isostasy and the surface of the Ice-Age Earth: The ICE-5G (VM2) model and GRACE. *Annual Review of Earth and Planetary Sciences*, *32*, 111–149.

Peltier, W. R., Argus, D. F., & Drummond, R. (2015). Space geodesy constrains ice-age terminal deglaciation: The global ICE-6G_C (VM5a) model. *Journal of Geophysical Research: Solid Earth*, *120*, 450–487. https://doi.org/10.1002/2014JB011176

Perrette, M., Landerer, F., Riva, R., Frieler, K., & Meinshausen, M. (2013). A scaling approach to project regional sea level rise and its uncertainties. *Earth System Dynamics*, *4*, 11–29. https://doi.org/10.5194/esd-4-11-2013

Roberts, C. D., Calvert, D., Dunstone, N., Hermanson, L., Palmer, M. D., & Smith, D. (2016). On the drivers and predictability of seasonal-to-interannual variations in regional sea level. *Journal of Climate*, *29*, 7565–7585. https://doi.org/10.1175/JCLI-D-15-0886.1

Rohmer, J., Le Cozannet, G., & Manceau, J.-C. (2019). Addressing ambiguity in probabilistic assessments of future coastal flooding using possibility distributions. *Climatic Change*, *155*(1), 95–109. https://doi.org/10.1007/s10584-019-02443-4

Sen Gupta, A., Jourdain, N. C., Brown, J. N., & Monselesan, D. (2013). Climate drift in the CMIP5 models. *Journal of Climate*, *26*, 8597–8615. https://doi.org/10.1175/JCLI-D-12-00521.1

Shepherd, T. G., Boyd, E., Calel, R. A., Chapman, S. C., Dessai, S., Dima-West, I. M., et al. (2018). Storylines: An alternative approach to representing uncertainty in physical aspects of climate change. *Climatic Change*, *151*(3-4), 555–571. https://doi.org/10.1007/s10584-018-2317-9

Slangen, A. B. A., Carson, M., Katsman, C. A., van de Wal, R. S. W., Koehl, A., Vermeersen, L. L. A., & Stammer, D. (2014). Projecting twenty-first century regional sea-level changes. *Climatic Change*, *124*, 317–332. https://doi.org/10.1007/s10584-014-1080-9

Spada, G., & Melini, D. (2019). SELEN^4 (SELEN version 4.0): A Fortran program for solving the gravitationally and topographycally self-consistent sea level equation in glacial isostatic adjustment modeling. *Geoscientific Model Development Discussion*, *12*(12), 5055-5075, https://www.geosci-model-dev-discuss.net/gmd-2019-183/; https://doi.org/10.5194/gmd-2019-183

Stammer, D., van de Wal, R. S. W., Nicholls, R. J., Church, J. A., Le Cozannet, G., Lowe, J. A., et al. (2019). Framework for high-end estimates of sea level rise for stakeholder applications. *Earth's Future*, *7*, 923–938. https://doi.org/10.1029/2019EF001163

Tamisiea, M. E., & Mitrovica, J. X. (2011). The moving boundaries of sea level change: Understanding the origins of geographic variability. *Oceanography*, *24*, 24–39. https://doi.org/10.5670/oceanog.2011.25

Taylor, K. E., Stouffer, R. J., & Meehl, G. A. (2012). An overview of CMIP5 and the experiment design. *Bulletin of the American Meteorological Society*, *93*, 485–498. https://doi.org/10.1175/BAMS-D-11-00094.1

Vousdoukas, M. I., Mentaschi, L., Voukouvalas, E., Verlaan, M., Jevrejeva, S., Jackson, L. P., & Feyen, L. (2018). Global probabilistic projections of extreme sea levels show intensification of coastal flood hazard. *Nature Communications*, *9*, 2360. https://doi.org/10.1038/s41467-018-04692-w

Wada, Y., van Beek, L. P. H., Weiland, F. C. S., Chao, B. F., Wu, Y. H., & Bierkens, M. F. P. (2012). Past and future contribution of global groundwater depletion to sea-level rise. *Geophysical Research Letters*, *39*, L09402. https://doi.org/10.1029/2012GL051230

Yin, J., Schlesinger, M. E., & Stouffer, R. J. (2009). Model projections of rapid sea-level rise on the northeast coast of the United States. *Nature Geoscience*, *2*, 262–266. https://doi.org/10.1038/NGEO462

References From the Supporting Information

Dziewonski, A. M., & Anderson, D. L. (1981). Preliminary reference earth model. *Physics of the Earth and Planetary Interiors*, *25*, 297–356. https://doi.org/10.1016/0031-9201(81)90046-7

Farrell, W. E., & Clark, J. A. (1976). On postglacial sea level. *Geophysical Journal of the Royal Astronomical Society*, *46*, 647–667. https://doi.org/10.1111/j.1365-246X.1976.tb01252.x

Lambeck, K. (1980). *The Earth's variable rotation: Geophysical causes and consequences* (pp. xi + 449). Cambridge, London, New York, New Rochelle, Melbourne, Sydney: Cambridge University Press.

Mitrovica, J. X., & Peltier, W. R. (1991). On postglacial geoid subsidence over the equatorial oceans. *J. Geophys. Res.*, *96*(B12), 20,053–20,071. https://doi.org/10.1029/91JB01284

Schotman, H. H. A. (2008). *Shallow-Earth rheology from glacial isostasy and satellite gravity (PhD thesis)*. Delft, The Netherlands: TU Delft.

Tegmark, M. (1996). An icosahedron-based method for pixelizing the celestial sphere. *The Astrophysical Journal*, *470*(2), L81–L84. https://doi.org/10.1086/310310

Wang, H., Xiang, L., Jia, L., Jiang, L., Wang, Z., Hu, B., & Gao, P. (2012). Load Love numbers and Green's functions for elastic Earth models PREM, iasp91, ak135, and modified models with refined crustal structure from Crust 2.0. *Computers & Geosciences*, *49*, 190–199. https://doi.org/10.1016/j.cageo.2012.06.022